

Investigating pre-eruptive magnetic properties at the footprints of erupting magnetic flux ropes

WENSI WANG,¹ JIONG QIU,² RUI LIU,^{1,3,4} CHUNMING ZHU,² KAI E YANG,⁵
QIANG HU,⁶ AND YUMING WANG^{1,3}

¹*CAS Key Laboratory of Geospace Environment, Department of Geophysics and Planetary Sciences
University of Science and Technology of China, Hefei, 230026, China*

²*Department of Physic, Montana State University, Bozeman, MT 59717, USA*

³*CAS Center for Excellence in Comparative Planetology, University of Science and Technology of
China
Hefei 230026, China*

⁴*Mengcheng National Geophysical Observatory, University of Science and Technology of China
Mengcheng 233500, China*

⁵*Institute for Astronomy, University of Hawaii at Manoa, Pukalani 96768, USA*

⁶*Department of Space Science and CSPAR, University of Alabama in Huntsville, Huntsville, AL
35805, USA*

ABSTRACT

It is well established that solar eruptions are powered by free magnetic energy stored in current-carrying magnetic field in the corona. It has also been generally accepted that magnetic flux ropes (MFRs) are a critical component of many coronal mass ejections (CMEs). What remains controversial is whether MFRs are present well before the eruption. Our aim is to identify progenitors of MFRs, and investigate pre-eruptive magnetic properties associated with these progenitors. Here we analyze 28 MFRs erupting within 45 deg from the disk center from 2010 to 2015. All MFRs' feet are well identified by conjugate coronal dimmings. We then calculate magnetic properties at the feet of the MFRs, prior to their eruptions, using Helioseismic and Magnetic Imager (HMI) vector magnetograms. Our results show that only 8 erupting MFRs are associated with significant non-neutralized electric currents, 4 of which also exhibit pre-eruptive dimmings at the foot-prints. Twist and current distributions are asymmetric at the two feet of these MFRs. The presence of pre-eruption dimmings associated with non-neutralized currents suggests the pre-existing MFRs. Furthermore, evolution of conjugate dimmings and electric currents within the foot-prints can provide clues about the internal structure of MFRs and their formation mechanism.

Corresponding author: Wensi Wang
minesnow@ustc.edu.cn

Keywords: sun, corona — magnetic flux rope — sunspot — flare

1. INTRODUCTION

Solar eruptions, such as prominence eruptions, solar flares and coronal mass ejections (CMEs), are the dominant contributor to adverse space weather at Earth. Now it is well established that these phenomena are powered by free magnetic energy, which is stored in current-carrying magnetic fields in the corona. What remains controversial is whether electric current is neutralized or not in the solar active regions (ARs) when integrating over the whole active region for each polarity individually. ARs are believed to be formed through subsurface flux tubes emerged from the solar interior (Fan 2009). The current flowing in an isolated magnetic flux tube can be divided into two parts: the so-called main (direct) currents, and shielding (return) currents (Melrose 1991; Parker 1996). Parker (1996) suggested that these isolated flux tubes are individually current-neutralized, which requires the main currents surrounded by shielding currents of equal amount and in opposite direction. However, Melrose (1991, 1995) argued that net currents can emerge from the solar interior. Longcope & Welsch (2000) further predicted that most return currents would be trapped below or at the photosphere.

The answer to current neutralization may have critical consequences for theoretical flare/CME models and pre-eruptive magnetic configuration. While it is a consensus that the key structure of the flare/CME models is a magnetic flux rope (MFR), the nature of the pre-eruptive configuration, a pre-existing MFR or a shear arcade, has been under intense debate. Many previous studies predicted that a current-carrying MFR can emerge from the solar convection zone into the corona, injecting the non-neutralized currents into the ARs (e.g. Leka et al. 1996; Titov & Démoulin 1999; Fan & Gibson 2004; Fan 2009; Démoulin & Aulanier 2010; Cheung & Isobe 2014). Török et al. (2014) modeled the emergence of a sub-photospheric current-neutralized MFR into the solar atmosphere. In their three-dimensional magnetohydrodynamic (MHD) simulation, a strong deviation from current neutralization was found at the end of emergence. Further, Dalmasse et al. (2015) investigated the distribution and neutralization of currents generated by photospheric horizontal flows in 3D, zero- β , MHD simulations. In their experiment, net currents would develop around the polarity inversion line (PIL), when photospheric plasma flows produced magnetic shear along the PIL.

Recently, more attention has been paid to investigate these theoretical considerations using uninterrupted high spatial-resolution data on vector magnetic fields provided by space instruments (e.g. the Helioseismic and Magnetic Imager on board Solar Dynamics Observatory, SDO/HMI, Pesnell et al. 2011). Georgoulis et al. (2012) performed a detailed observational study of electric current patterns in two ARs. They found that only the ARs with well-formed PILs contain stronger non-neutralized

current patterns per polarity. Liu et al. (2017) indicated that the degree of current neutralization would be a better proxy for assessing the CME productivity of the ARs by conducting a pilot observational study of four ARs. Later, this relationship has been explored in larger samples (Vemareddy 2019; Kontogiannis et al. 2019; Avallone & Sun 2020). Avallone & Sun (2020) had investigated the degree of current neutralization in 30 ARs (15 flare-active and 15 flare-quiet). Their results confirmed that most flare-active ARs own non-neutralized currents, while flare-quiet ARs exhibit the characteristic of neutralization.

Those observations, however, did not clarify whether non-neutralized currents in active regions are necessarily signatures of a magnetic flux rope (MFR) that are present before the eruption. To understand formation mechanisms of non-neutralized currents and verify previous models and simulations, it is necessary to investigate electric currents of MFRs in the observations. However, the technology of direct measuring the coronal magnetic field is still immature, thus it poses a major challenge to observational investigation of MFRs' magnetic properties. According to 3D extension of the standard flare models and numerical models (e.g. Gosling 1990; Moore et al. 2001; Janvier et al. 2014; Aulanier & Dudík 2019), magnetic reconnection occurring around and below the erupting MFR should produce J/Z-shaped flare ribbons, with the ribbon hooks marking the boundary of the photospheric feet of the erupting MFR. Barczynski et al. (2020) attempted to search possible regions of MFRs' feet based on these characteristics. Unfortunately, less than half flares in their sample were observed with clear ribbon hooks, which are considered as boundary of the footpoints.

To specifically map the MFR's feet, more observational features are required. The ejection of emitting plasma will cause transient darkening of the areas in the eruptive region, named as coronal dimmings or transient coronal hole (Harrison & Lyons 2000; Harra & Sterling 2001). Particularly, conjugate coronal dimmings that occur in the vicinity of flare ribbons and are located in photospheric fields of opposite polarities can well map the MFR's feet (Webb et al. 2000; Qiu et al. 2007; Hu et al. 2014; Cheng & Qiu 2016; Qiu & Cheng 2017; Wang et al. 2017, 2019). In addition, Qiu & Cheng (2017) and Wang et al. (2019) observed two eruptive events with clear conjugate dimmings that appeared several hours before the eruptions. Therefore, conjugate coronal dimmings are a good candidate to help identify MFRs' foot-prints. In particular, if pre-eruptive dimmings are present at the same locations, they will help diagnose the dynamic and magnetic evolution of coronal structures, which are likely MFRs, before the MFR eruption.

Here we conduct a statistical study to explore pre-eruptive magnetic properties of erupting MFRs. We quantify magnetic properties at the feet of 28 MFRs prior to their eruptions using high-quality vector magnetograms from HMI. In the following section, we will briefly introduce the selection of eruptive events, our method of footpoints identification, measurements of magnetic properties at the footprints of MFRs, and

uncertainties of MFRs properties estimated in this study. The statistical results will be shown in the Section 3 and Section 4. Summaries and conclusions are given in Section 5.

2. DATA AND METHODOLOGY

2.1. Dataset

According to previous flare/CME models (e.g. Moore et al. 2001; Janvier et al. 2014) and observational studies (e.g. Hu et al. 2014; Cheng & Qiu 2016; Qiu & Cheng 2017; Wang et al. 2017, 2019), two-ribbon flares with conjugate dimmings will be good candidates for identifying the MFRs' footpoints, and subsequently measuring their magnetic properties. We have examined 400 two-ribbon flares of GOES class C5.0 and larger from a database *RibbonDB* (Kazachenko et al. 2017), which includes all flares of GOES class C1.0 and larger, observed by the Atmospheric Imaging Assembly (AIA; Lemen et al. 2012) onboard SDO from 2010 to 2016. To minimize projection effects, we choose flare events that occur within 45° from the central meridian. Meanwhile, only flares of GOES class larger than C5.0 and smaller than X2.0 are considered. Then only 52 flare events are retained. Our preliminary analysis of these events shows that about 28 events exhibit evident conjugate dimmings. We hence select the 28 events with conjugate dimmings to conduct the statistical study.

Table 1 provides observational properties of the 28 eruptive events. All studied events are associated with CMEs observed by the Solar Terrestrial Relations Observatory (STEREO; Kaiser et al. 2008) and/or the Large Angle and Spectrometric Coronagraph Experiment (LASCO). From STEREO and LASCO observations, most CMEs are showing classical three-part structures or twisted loop-like structures, implying the existence of MFRs. Half of them are halo CMEs when viewed from Earth, and 7 among them are associated with magnetic clouds (MCs) observed at 1 AU. Before the eruptions, some plasma proxies for MFRs, including sigmoids, hot channels, filaments, and expanding coronal loops, are well visible for most events.

2.2. Identification of erupting MFRs' footpoints

Many previous studies (Webb et al. 2000; Qiu et al. 2007; Cheng & Qiu 2016; Qiu & Cheng 2017; Wang et al. 2017, 2019) indicated that conjugate dimmings located in magnetic fields of opposite polarities map the MFR's feet. Statistical studies of coronal dimmings (Dissauer et al. 2018a,b, 2019) suggested that coronal dimmings often occur in multiple extended areas, due to projection or interaction of the large scale structure of the erupting MFR. Their studies also found that only small parts of the coronal dimming map the feet of the original MFR, and their edges are difficult to identify automatically. Therefore, in the past, combined manual and semi-automatic detection methods were employed to determine feet-related dimming regions (e.g. Qiu & Cheng 2017; Wang et al. 2017, 2019; Xing et al. 2020).

In this study, we have developed a novel automated algorithm to detect footpoints of erupting MFRs, based on theoretical concepts and observational characteristics

of MFRs. This method has been improved upon our previous detection method of coronal dimmings (see Wang et al. 2017, 2019). First of all, our method will analyze seven EUV passbands of AIA observations synchronously to seek possible coronal dimming regions. This step will guarantee the detected dimmings are due to mass evacuation related to eruption or expansion, rather than the change in the plasma temperature. Then all detected regions will be projected onto the preflare HMI vector magnetogram to check their magnetic polarity and connectivity. In this process, the dimmed regions that are co-spatial with the magnetic field of mixed polarity and conflicting connectivity are discarded. According to 3D extension of flare/CME models (e.g. Moore et al. 2001; Janvier et al. 2014), feet-related dimmings tend to appear in the vicinity of flare ribbons. In the next step, our method will examine the location of detected dimmings, selecting the dimmed regions that occur along the two flare ribbons. The flare ribbons are detected in the AIA 1600 channel using the method from Qiu et al. (2007). Finally, two boundaries of conjugate dimmings will be determined. More detailed information can be found in the Appendix A.

2.2.1. *Pre-eruption and post-eruption dimmings*

To estimate the specific areas of the expanding or erupting MFRs' feet, we quantify the evolution of conjugate dimmings. Many studies had indicated that some coronal dimming signatures may be caused by projection effects, when coronal loops evolve and change their orientations (Harvey & Recely 2002; Harra et al. 2007; Qiu et al. 2007; Scholl & Habbal 2008). To minimize such projection effects, we track evolution of dimmings in the AIA 304 passband. We then project the dimming pixels onto the HMI vector magnetogram half an hour before each flare and sum up the magnetic flux within the dimming regions to calculate the dimming fluxes. The results show that conjugate dimmings will appear before or after the onset of flares, which are termed pre-eruption dimmings (Figure 1) or post-eruption dimmings (Figure 2). In this study, the pre-eruption dimmings appear at least one hour before the onset of flare. According to previous studies about conjugate dimming fluxes (e.g. Qiu et al. 2007; Hu et al. 2014; Wang et al. 2017, 2019), the order of magnitude of dimming fluxes are around 10^{20-22} Mx. Here the occurrence of dimmings is defined by the moment when the value of dimming fluxes becomes larger than 10^{19} Mx.

Our results show that most pre-eruption dimmings will expand in area before the eruption and shrink during the eruption (Figure 1). It is worth noting that dimming fluxes are calculated using the same pre-flare HMI magnetogram (half an hour before the onset of the flare). For example, the 20110930 event, dimming fluxes rapidly increase and reach a plateau, which lasts about 1.5 hours. The dimming fluxes start to decrease several minutes before the onset of the flare (vertical dashed line in Figure 1 (a)). But for several events, the dimming fluxes grow slowly before the eruption, e.g. the 20130830 event (see Figure 1 (b)). The negative dimming fluxes in the 20130830 event increase fast after the onset of the flare. For the 20110621 event, dimming fluxes start to rise three hours before the flare and continue to rise during the eruption.

In this study, we neglect pixels undergoing transient dimmings, which are mainly detected during the period of rapid changes; but focus on dimmed pixels that persist for a long time, mainly detected during the relatively stable stage in the light-curve of dimming fluxes. As a result, we identify two stationary dimming regions during the whole eruption process. Despite the evolution of coronal dimmings, the two stationary regions are considered as the 'core' feet of the MFR, from which the magnetic properties of the MFR are investigated. For examples, for the 20110930 and 20120614 event, we select all dimming pixels detected during the plateau of fluxes. For the 20110621 event and 20130830 event, we select all dimming pixels when the fluxes grow to 40% of its maximum. The identified footpoints of these four events are shown in the Figure 3 (white contours). In our sample of pre-eruption dimmings, we find that, when flare occurs, flare ribbons tend to cover part of dimming areas (see Figure 3 (red contours)), explaining the reduction of dimming fluxes during the eruption.

Our results show that the post-eruption dimmings always experience a stage of rapid expansion in area, followed by a stage of relatively stable and slow growth (Figure 2). For example, in the 20120310 event, the negative dimming flux increases rapidly after the onset of the flare (Figure 2 (d)). For the post-eruption dimmings, we select all dimming pixels detected after the period of rapid growth. Then we consider that these pixels map the MFR footpoints. The white contours in Figure 4 denote the conjugate footpoints of the MFR identified with this method. For post-eruption dimmings, the flare ribbons also cover part of the dimming areas (Figure 4). In this way, footpoints of 28 MFRs are all well identified.

Table 1. Overview of Eruptions

No.	Date	AR		Flare		Dimming		CME	MC	MFR identity
		NOAA	Location	class	Onset	Onset	Label			
1	20100807	11093	N12E31	M1.0	17 : 55	18 : 35	Post	Halo	–	Double – Decker filament
2	20110307	11166	N11E13	M1.7	13 : 45	14 : 10	Post	Yes	–	Hot channel
3	20110621	11236	N17W21	C7.7	01 : 18	*22 : 02	Pre	Yes	–	Sigmoid – like filament
4	20110802	11261	N16W22	M1.4	05 : 19	05 : 07	Post	Halo	–	Hot channel
5	20110930	11305	N13E02	M1.3	18 : 55	17 : 03	Pre	Yes	–	Expanding coronal structure
6	20120309	11429	N17W13	M6.3	03 : 22	03 : 40	Post	Halo	–	Hot channel
7	20120310	11429	N18W27	M8.4	17 : 15	17 : 30	Post	Halo	–	Hot channel
8	20120614	11504	S17W00	M1.0	12 : 52	08 : 00	Pre	Halo	Yes	Expanding coronal structure
9	20120712	11520	S17W08	X1.4	15 : 37	16 : 18	Post	Halo	Yes	Hot channel
10	20130206	11667	N22W00	C8.7	00 : 04	00 : 10	Post	Yes	–	Filament
11	20130411	11719	N10W01	M6.5	06 : 55	06 : 01	Pre	Halo	Yes	Hot channel
12	20130517	11748	N12E22	M3.2	08 : 43	08 : 52	Post	Halo	–	Hot channel
13	20130812	11817	S22E10	M1.5	10 : 21	10 : 42	Post	Yes	–	
14	20130817	11818	S07W32	M3.3	18 : 16	18 : 40	Post	Yes	–	Twisted loops
15	20130830	11836	N12E28	C8.3	02 : 04	01 : 04	Pre	Yes	–	Expanding coronal structure
16	20131013	11865	S22E05	M1.7	00 : 12	00 : 32	Post	Yes	–	
17	20140131	11968	N09E29	M1.1	15 : 32	15 : 40	Post	Yes	–	
18	20140320	12010	S15E27	M1.7	03 : 42	03 : 52	Post	Halo	–	
19	20140730	12127	S08E34	C9.0	16 : 00	16 : 10	Post	Yes	–	
20	20140801	12127	S09E08	M1.5	17 : 55	18 : 22	Post	Halo	–	
21	20140825	12146	N09W47	M2.0	14 : 46	14 : 01	Pre	Yes	–	Expanding coronal structure
22	20140825	12146	N09W47	M3.9	20 : 06	19 : 35	Pre	Halo	–	Expanding coronal structure
23	20140908	12158	N16E26	M4.5	23 : 12	22 : 31	Pre	Halo	Yes	Sigmoid
24	20140910	12158	N15E02	X1.6	17 : 21	16 : 02	Pre	Halo	Yes	Sigmoid
25	20140921	12166	N11W55	C5.2	11 : 31	11 : 24	Post	Yes	Yes	
26	20141220	12242	S18W42	X1.8	0 : 11	00 : 30	Post	Yes	–	
27	20150622	12371	N13W14	M6.5	17 : 39	17 : 59	Post	Halo	–	Hot channel
28	20151104	12443	N06W10	M3.7	13 : 31	13 : 45	Post	Halo	Yes	

NOTE— Table 1 shows detailed information of 28 flare events. The dimmings are marked as "pre" when it appeared at least half hour before the start time of the associated flare. The dimmings are marked as "post" when it appeared after the onset of flares. * the onset of dimmings occurred one day before the date of the flare.

2.3. Measuring pre-eruptive magnetic properties of MFRs

2.3.1. Magnetic flux

By projecting the identified footpoints onto the pre-flare HMI vector magnetogram, we can estimate pre-eruptive magnetic properties of erupting MFRs. In this study, we use the Space-weather HMI Active Region Patch (SHARP) data series, hmi.sharp_cea_720s¹, which is disambiguated and deprojected to the heliographic coordinates with a Lambert (cylindrical equal area) projection method, resulting in a pixel scale of 0.36 Mm (Bobra et al. 2014). For each event, we select one pre-flare HMI vector magnetogram, about half an hour before the onset of the flare, to calculate magnetic fluxes and electric currents. The net magnetic flux (Φ_{net}) can be estimated by summing up B_z within the identified footpoint regions. The uncertainties of magnetic fluxes are estimated by error propagations:

$$\delta_{\Phi} = \sqrt{\sum_S (\delta_{B_z})^2}$$

where δ_{B_z} is directly taken from the uncertainties of the HMI data (Hoeksema et al. 2014).

2.3.2. Electric current

In theoretical models, for a coherent MFR, the electric current density \mathbf{j} near its center will flow in one direction, termed as "direct current" (DC), while the \mathbf{j} around the MFR periphery must flow in the opposite direction, termed as "return current" (RC) (Liu et al. 2017; Sun & Cheung 2020). The vertical current density j_z and the net current I_z can be estimated from the HMI vector magnetogram using the Ampere's law and Stokes theorem:

$$j_z = (\nabla \times \mathbf{B})_z / \mu_0$$

$$I_z = \frac{1}{\mu_0} \int_S j_z dS = \frac{1}{\mu_0} \oint_C B_h \cdot dl$$

where S is the area of identified footpoints, C is the perimeter of S , and $\mu_0 = 4\pi \times 10^{-7} \text{Hm}^{-1}$.

Following the calculation of current neutralization from Liu et al. (2017); Avallone & Sun (2020); Sun & Cheung (2020), the index $R_z = |I_z^{DC} / I_z^{RC}|$ is utilized to determine whether the MFR contains non-neutralized currents or not. For each event, I_z^{DC} and I_z^{RC} are computed for the MFR's footpoints by integrating j_z values of a different sign separately. In order to determine the sign of I_z^{DC} , we search for dominate sign of j_z / B_z in the MFR's feet. Figure 5 shows electric current density maps for four events as examples. For the 20110930 and 20120614 events, the sign of I_z^{DC} for each

¹ http://jsoc.stanford.edu/HMI/Vector_products.html

foot is very obvious. But for the 20120310 and 20140921 event, it will be difficult to determine the sign of I_z^{DC} .

The HMI vector field has an unavoidable 180° ambiguity in the transverse field direction. For the disambiguation of HMI data, the minimum energy algorithm (Metcalf 1994; Metcalf et al. 2006; Leka et al. 2009), which is based on a linear force-free field, is employed. This method may not well disambiguate for weak field regions, where the signal is dominated by noise. That will directly affect our calculation of current neutralization, since many footpoints locate in the weak-field regions. In some previous studies (e.g. Avallone & Sun 2020), they only considered the regions where the absolute value of the magnetic field is stronger than 200 G. But the value of electric current will be dramatically reduced when removing weak-field pixels. More detailed comparison between original electric currents and the currents that are calculated by only sum up strong-field pixels can be found in the Appendix B.

After many attempts, we find that averaging j_z over several hours will largely minimize the effect of low signal-to-noise pixels in the calculation. Comparing with the original electric current density maps (Figure 5 (a2) to (d2)), most weak-field pixels are eliminated in the average maps (Figure 5 (a3) to (d3)). To further display temporal evolution of these pixels, we cut out four weak-field regions (50×50 pixel) from four events (see four squares in the Figure 5). For the weak-field pixels, the plus or minus sign of j_z always appear alternately. Therefore, averaging current density maps over a period of time will well eliminate these noise-like pixels. In this study, we average j_z over a period of two hours, noting that the timescale of the evolution of the photospheric field is several hours.

The results indicate two MFR populations, one carrying net currents (at least one foot with the value of R_z larger than 2.0), and the other carrying neutralized currents. We find 8 out of 28 MFRs contain significant non-neutralized currents. For example, the R_z for one foot of 20110930 event is about 7.0, while the R_z in the two feet of the 20140921 event ranges from 1.0 to 1.2. The histogram of R_z for the 28 MFRs is shown in the Figure 6. For each foot, the number of events first decreases with the increasing R_z , and then flattens at around 1.8 to 2.0. Previous studies provided the R_z for the active region ranging from 1.1 to 2.0 (Liu et al. 2017; Avallone & Sun 2020). We suggest 1.8 – 2.0 as an possible empirical threshold to distinct the MFRs with or without net currents when considering the average value of R_z in two footpoints.

Similar to magnetic fluxes, the uncertainties of electric currents are also estimated by error propagations:

$$\delta_I = \sqrt{\sum_S (\delta_{j_z})^2}$$

But electric currents are calculated from the aforementioned average j_z maps. Then we consider the standard deviation of the variation of j_z during two hours as δ_{j_z} . More information about the uncertainties of j_z can be found in the Appendix B. For the $\delta_{I_z^{DC}}$ and $\delta_{I_z^{RC}}$, we only consider pixels carrying the current with the same polarity

of I_z^{DC} or I_z^{RC} . The uncertainties of the degree of current neutralization (δ_{R_z}) is also given by error propagations:

$$\delta_{R_z} = R_z \sqrt{\left(\frac{\delta_{I_z^{DC}}}{I_z^{DC}}\right)^2 + \left(\frac{\delta_{I_z^{RC}}}{I_z^{RC}}\right)^2}$$

3. THE PRE-ERUPTIVE MAGNETIC PROPERTIES OF ERUPTING MFRS

Table 2 and Table 3 list the properties measured at two feet of each of the 28 MFRs, including the net magnetic flux (Φ_{net}), the net electric current (I_z^{net}), the direct current (I_z^{DC}), the return current (I_z^{RC}), and the degree of current neutralization (R_z). For each event, magnetic fluxes are estimated from the HMI vector magnetogram obtained half an hour before the eruption, while electric currents are calculated using the current density map averaging over two hours before the eruption. The Φ_{net} of MFRs is around 10^{20-21} Mx, comparable to toroidal fluxes calculated from magnetic clouds (Hu et al. 2014). The I_z^{net} of MFRs is around 10^{11-12} A, in the same order of magnitude as the current calculated from ends of sigmoids (Cheng & Ding 2016). The I_z^{DC} in their study is about an order of magnitude higher than ours, probably because they arbitrarily choose a rectangular region as the footpoints. In addition, the I_z in our study is derived by averaging the measurements in two hours. In the tables, the sign of footpoints represents the sign of magnetic polarities, positive (+) or negative (-). Furthermore, we also distinguish the two feet as the leading footpoint (L) and the trailing footpoint (T), according to the direction of solar rotation.

3.1. *The footpoints identified by pre-eruption conjugate dimmings*

In our sample of 28 events, we find 9 events with obvious pre-eruption conjugate dimmings, which appear at least one hour before the onset of the flare (see Table 1). The observational signatures of the MFR, e.g. expanding coronal structures (Wang et al. 2019), sigmoid-like filaments (Zhou et al. 2017), sigmoids and hot channels (Cheng & Ding 2016), are observed for each event before the eruption. For these events, conjugate dimmings evolve simultaneously with the MFR-like structures, suggesting that the pre-eruption dimmings map the feet of the MFR-like structures.

Here we show a typical case about the pre-eruption dimmings, the 20120614 event. The eruption of interest is associated with an M1.9 flare, which is captured by SDO and STEREO. The observations from STEREO-B/EUVI reveal a gradual expansion of a coronal structure lasting for more than five hours before the onset of the flare (Figure 7 (a1) to (a3)), which finally evolved into a halo CME (Figure 7 (b)). The average brightnesses for the two identified footpoint regions evolve simultaneously with the expanding coronal structure (Figure 7 (c) and (d)). More detailed investigation about this event can be found in our previous study (Wang et al. 2019). In our sample, most pre-eruption dimmings evolve simultaneously with expanding structures, which finally erupt as a CME.

We further compare dimming areas detected before and after the onset of flares. For most events, dimming areas detected before the flare are always larger than dimming areas detected after the flare. Figure 8 shows the comparison for the aforementioned four events. For 20110930 and 20120614 event, dimming areas detected before the flare (blue contours in the Figure 8 (a) and (d)) completely cover dimming areas detected after the flare (green contours in the Figure 8 (a) and (d)). For 20110621

event, two areas are nearly the same (Figure 8 (c)). For 20130830 event, as one exception, the dimming area after the flare is larger than the area before the flare. More interestingly, for 20110930 event, flare ribbons occur inside two dimming areas (Figure 3 (a)), causing the reduction of dimming fluxes (Figure 1 (a)). Yet after the flare, dimming occurs again in the region covered by flare ribbons, hence the dimming fluxes grow again after the flare. (Figure 1 (a)).

Table 2 shows quantitative measurements of magnetic properties within the footpoints identified by pre-eruption conjugate dimmings. The $|\Phi_{net}|$ in the footpoints range from 3.62×10^{20} to 50.95×10^{20} Mx and the $|I_z^{net}|$ range from 0.14×10^{11} to 19.12×10^{11} A. The maximum of $|I_z^{DC}|$ is about 41.91×10^{11} A, and the minimum is about 2.65×10^{11} A, much higher than the range of $|I_z^{net}|$. But the range of R_z is from 1.0 to 7.0. The results show that four events are associated with non-neutralized currents ($R_z > 2.0$), marked in bold font in Table 2. The R_z of the other events are around 1.0 to 1.5.

3.2. The footpoints identified by post-eruption conjugate dimmings

The rest 19 events are all associated with obvious post-eruption conjugate dimmings (see Table 1). For half of the events, we did not find obvious signatures of MFRs

Table 2. The pre-eruptive magnetic properties of pre-eruption dimming events

No.	Date	FP		Φ_{net} (10^{20} Mx)	I_z^{net} (10^{11} A)	I_z^{DC} (10^{11} A)	I_z^{RC} (10^{11} A)	R_z
		Sign	Type					
3	20110621	+	<i>T</i>	13.56 ± 0.02	0.53 ± 1.82	30.17 ± 1.26	-29.64 ± 1.24	1.0 ± 0.1
		-	<i>L</i>	-12.70 ± 0.03	-1.60 ± 1.68	-23.43 ± 1.07	21.83 ± 1.06	1.1 ± 0.1
5	20110930	+	<i>T</i>	5.42 ± 0.01	-4.38 ± 1.49	-16.33 ± 0.91	11.95 ± 0.78	1.4 ± 0.1
		-	<i>L</i>	-13.77 ± 0.21	7.64 ± 1.06	8.92 ± 0.42	-1.28 ± 0.21	7.0 ± 1.2
8	20120614	+	<i>L</i>	40.00 ± 0.03	11.52 ± 0.87	13.60 ± 0.28	-2.08 ± 0.15	6.5 ± 0.5
		-	<i>T</i>	-30.67 ± 0.02	-19.12 ± 1.32	-31.47 ± 0.70	12.35 ± 0.61	2.6 ± 0.1
11	20130411	+	<i>T</i>	8.62 ± 0.03	-0.62 ± 1.80	-2.65 ± 1.23	2.58 ± 1.21	1.0 ± 0.7
		-	<i>L</i>	-5.91 ± 0.01	0.79 ± 0.93	5.84 ± 0.32	-5.05 ± 0.36	1.2 ± 0.1
15	20130830	+	<i>T</i>	21.24 ± 0.08	2.51 ± 1.61	23.04 ± 0.99	-20.53 ± 0.96	1.1 ± 0.1
		-	<i>L</i>	-15.85 ± 0.07	0.14 ± 2.08	44.71 ± 1.64	-44.57 ± 1.64	1.0 ± 0.1
21	20140825	+	<i>T</i>	4.21 ± 0.02	-4.54 ± 1.04	-8.45 ± 0.45	3.91 ± 0.37	2.2 ± 0.2
		-	<i>L</i>	-6.24 ± 0.01	3.53 ± 0.82	6.74 ± 0.26	-3.21 ± 0.26	2.1 ± 0.2
22	20140825	+	<i>T</i>	3.62 ± 0.02	-0.84 ± 1.19	-7.41 ± 0.55	6.57 ± 0.52	1.1 ± 0.1
		-	<i>L</i>	-5.25 ± 0.01	1.18 ± 0.84	4.62 ± 0.27	-3.44 ± 0.28	1.3 ± 0.1
23	20140908	+	<i>L</i>	50.95 ± 0.04	-16.75 ± 1.01	-23.71 ± 0.44	6.96 ± 0.38	3.4 ± 0.2
		-	<i>T</i>	-44.39 ± 0.04	8.01 ± 1.69	41.91 ± 1.13	-33.93 ± 1.02	1.2 ± 0.1
24	20140910	+	<i>L</i>	19.64 ± 0.02	-5.71 ± 1.23	-16.47 ± 0.50	10.76 ± 0.57	1.5 ± 0.1
		-	<i>T</i>	-29.38 ± 0.02	10.50 ± 1.55	33.48 ± 0.95	-22.99 ± 0.87	1.5 ± 0.1

NOTE—Table 2 shows the properties of pre-eruption dimming events. The '+'/'-' in the table represents the footpoints of positive/negative magnetic polarities respectively, and 'L/T' represent the leading/trailing footpoints. The footpoints with non-neutralized current are in bold font.

before the eruption. For most events, dimmings appear several minutes or dozens of minutes after the onset of flares. The dimmings always undergo a rapid rise phase followed by a long stable phase (see Figure 2). As flare/CME models predicted, most post-eruption conjugate dimmings appear in the two end of flare ribbons. For example, the 20140921 event, two dimmings are located along the two flare ribbons (Figure 4 (b)). Some dimmings even appear inside the flare ribbons. For example, the 20120310 event, flare ribbons cover the most part of dimming areas (Figure 4 (d)).

Table 3 shows quantitative measurements of magnetic properties within the footpoints identified by post-eruption conjugate dimmings. The $|\Phi_{net}|$ in the footpoints range from 1.96×10^{20} to 42.74×10^{20} Mx and the $|I_z^{net}|$ range from 0.02×10^{11} to 11.52×10^{11} A. The maximum of $|I_z^{DC}|$ is about 55.49×10^{11} A, and the minimum is about 3.42×10^{11} A, much higher than the range of $|I_z^{net}|$. These values are similar to the results from the pre-eruption dimming events. But the range of R_z is smaller than that of the pre-eruption dimming events, from 1.0 to 3.6. Only 4 of 19 events are associated with non-neutralized currents ($R_z > 2.0$), marked in bold font in Table 3. The R_z for most events are around 1.0 to 1.6.

Table 3. The pre-eruptive magnetic properties of post-eruption dimming events

No.	Date	FP		Φ_{net} (10^{20} Mx)	I_z^{net} (10^{11} A)	I_z^{DC} (10^{11} A)	I_z^{RC} (10^{11} A)	R_z
		Sign	Type					
1	20100807	+	<i>T</i>	4.90 ± 0.02	-0.11 ± 1.31	-8.67 ± 0.64	8.56 ± 0.65	1.0 ± 0.1
		-	<i>L</i>	-6.55 ± 0.02	-0.02 ± 1.15	-7.32 ± 0.54	7.30 ± 0.50	1.0 ± 0.1
2	20110307	+	<i>T</i>	4.62 ± 0.02	-2.86 ± 1.31	-10.31 ± 0.65	7.45 ± 0.64	1.4 ± 0.2
		-	<i>L</i>	-7.01 ± 0.02	0.21 ± 1.29	10.18 ± 0.62	-9.97 ± 0.60	1.0 ± 0.1
4	20110802	+	<i>T</i>	13.62 ± 0.01	11.52 ± 0.91	15.93 ± 0.36	-4.41 ± 0.27	3.6 ± 0.2
		-	<i>L</i>	-8.00 ± 0.02	-4.28 ± 1.16	-11.68 ± 0.64	7.39 ± 0.50	1.6 ± 0.1
6	20120309	+	<i>L</i>	17.23 ± 0.03	-5.34 ± 1.48	-19.77 ± 0.82	14.43 ± 0.80	1.4 ± 0.1
		-	<i>T</i>	-17.58 ± 0.03	7.35 ± 1.45	21.69 ± 0.87	-14.34 ± 0.79	1.5 ± 0.1
7	20120310	+	<i>L</i>	10.31 ± 0.04	2.19 ± 1.61	23.84 ± 0.97	-21.65 ± 0.91	1.1 ± 0.1
		-	<i>T</i>	-30.79 ± 0.03	8.44 ± 1.46	26.87 ± 0.82	-18.43 ± 0.78	1.5 ± 0.1
9	20120712	+	<i>L</i>	42.74 ± 0.03	2.41 ± 1.87	55.49 ± 1.34	-53.08 ± 1.32	1.1 ± 0.0
		-	<i>T</i>	-34.46 ± 0.04	-0.86 ± 1.84	-49.74 ± 1.26	48.88 ± 1.28	1.0 ± 0.0
10	20130206	+	<i>T</i>	14.03 ± 0.03	2.38 ± 1.41	15.36 ± 0.73	-12.98 ± 0.76	1.2 ± 0.1
		-	<i>L</i>	-3.76 ± 0.02	-1.81 ± 1.42	-12.40 ± 0.78	-10.59 ± 0.76	1.2 ± 0.1
12	20130517	+	<i>L</i>	11.90 ± 0.02	-1.95 ± 1.09	-10.37 ± 0.45	8.42 ± 0.45	1.2 ± 0.1
		-	<i>T</i>	-11.39 ± 0.05	1.42 ± 1.78	30.15 ± 1.19	-28.74 ± 1.19	1.1 ± 0.1
13	20130812	+	<i>L</i>	3.42 ± 0.01	-1.78 ± 0.79	-3.95 ± 0.24	2.17 ± 0.23	1.8 ± 0.2
		-	<i>T</i>	-4.81 ± 0.01	2.43 ± 0.86	3.43 ± 0.32	-1.01 ± 0.24	3.4 ± 0.9
14	20130817	+	<i>L</i>	2.03 ± 0.01	1.58 ± 0.93	4.12 ± 0.30	-2.53 ± 0.33	1.6 ± 0.2
		-	<i>T</i>	-8.16 ± 0.02	-0.48 ± 1.19	-8.62 ± 0.54	8.13 ± 0.53	1.1 ± 0.1
16	20131013	+	<i>L</i>	5.82 ± 0.02	2.77 ± 1.14	8.40 ± 0.49	-5.63 ± 0.47	1.5 ± 0.2
		-	<i>T</i>	-8.87 ± 0.02	-9.58 ± 1.23	-16.39 ± 0.63	6.81 ± 0.51	2.4 ± 0.2
17	20140131	+	<i>T</i>	2.47 ± 0.03	-0.06 ± 1.44	-8.47 ± 0.80	8.41 ± 0.76	1.0 ± 0.1
		-	<i>L</i>	-1.96 ± 0.02	0.06 ± 1.39	8.73 ± 0.73	-8.67 ± 0.70	1.0 ± 0.1
18	20140320	+	<i>L</i>	8.22 ± 0.02	0.47 ± 1.27	9.96 ± 0.60	-9.49 ± 0.61	1.1 ± 0.1
		-	<i>T</i>	-12.90 ± 0.02	-1.92 ± 0.93	-6.18 ± 0.35	4.26 ± 0.31	1.5 ± 0.1
19	20140730	+	<i>L</i>	10.47 ± 0.02	-1.02 ± 1.18	-12.04 ± 0.56	11.02 ± 0.50	1.1 ± 0.1
		-	<i>T</i>	-8.19 ± 0.02	0.89 ± 1.31	8.25 ± 0.65	-7.36 ± 0.70	1.1 ± 0.1
20	20140801	+	<i>L</i>	8.80 ± 0.01	1.52 ± 1.30	13.56 ± 0.46	-12.04 ± 0.67	1.1 ± 0.1
		-	<i>T</i>	-6.72 ± 0.01	1.15 ± 1.13	7.27 ± 0.50	-6.12 ± 0.63	1.2 ± 0.2
25	20140921	+	<i>T</i>	4.31 ± 0.02	1.08 ± 1.19	7.67 ± 0.55	-6.59 ± 0.52	1.2 ± 0.1
		-	<i>L</i>	-5.64 ± 0.01	0.05 ± 0.89	3.98 ± 0.30	-3.93 ± 0.29	1.0 ± 0.1
26	20141220	+	<i>L</i>	15.87 ± 0.02	3.01 ± 1.55	19.08 ± 0.90	-16.08 ± 0.86	1.2 ± 0.1
		-	<i>T</i>	-33.19 ± 0.03	-2.81 ± 1.42	-29.58 ± 0.77	26.77 ± 0.76	1.1 ± 0.0
27	20150622	+	<i>T</i>	19.74 ± 0.02	-8.85 ± 1.04	-17.63 ± 0.46	8.79 ± 0.35	2.0 ± 0.1
		-	<i>L</i>	-27.67 ± 0.02	5.77 ± 1.69	32.75 ± 1.02	-26.98 ± 1.08	1.2 ± 0.1
28	20151104	+	<i>T</i>	8.93 ± 0.01	1.50 ± 1.33	12.45 ± 0.67	-10.97 ± 0.66	1.1 ± 0.1
		-	<i>L</i>	-8.07 ± 0.01	-1.01 ± 1.88	-23.57 ± 1.33	22.55 ± 1.36	1.1 ± 0.1

NOTE—Table 3 shows the pre-eruptive magnetic properties of post-eruption dimming events. Similar to the Table 2

4. THE CHARACTERISTIC OF MFR WITH NON-NEUTRALIZED CURRENT

In the entire sample of 28 events, only 8 events are associated with significant non-neutralized currents before eruptions (bold font in Table 2 and Table 3). Direct comparison between properties of the MFRs with or without net currents are given in the Figure 9 and Figure 10. For both signs of footpoints, we find a high correlation between the magnetic flux Φ_{net} in the two footpoints (Figure 9(a1)), the cross-correlation coefficient being 0.82 for the whole sample, 0.94 for the MFRs with non-neutralized currents, and 0.72 for the MFRs with neutralized currents. When considering the leading/trailing footpoint, the coefficient is slightly higher. The ratio of the fluxes in the two footpoints is close to one. We also find the direct currents I_z^{DC} in the two footpoints are comparable and strongly correlated (Figure 9(a2)). These results suggest that our method has successfully identified conjugate footpoints of MFRs. However, when considering the leading/trailing footpoints, the coefficient for the direct currents becomes smaller, especially for the MFRs with non-neutralized currents (Figure 9(b2)). Larger deviations are found in the net currents I_z^{net} for the MFRs with non-neutralized currents (Figure 9(a3)(b3)) and the degree of current neutralization R_z for all MFRs (Figure 9(a4)(b4)).

The distributions of magnetic properties from two MFR categories, with or without net current, is shown in the Figure 10. No statistically significant difference is found between two populations in magnetic fluxes and direct currents. When considering the leading/trailing footpoints, the results are similar. But the distribution of the net current I_z^{net} is quite different between two populations. Most I_z^{net} for the MFRs with non-neutralized currents (blue part in the Figure 10 (b1) to (b4)) are larger than 5×10^{11} A, while I_z^{net} for the MFRs with neutralized currents (red part in the Figure 10 (b1) to (b4)) distributes in 1×10^{11} to 5×10^{11} A. Moreover, similar distributions are found in the leading and trailing footpoints for I_z^{net} , especially for the MFRs with non-neutralized currents.

In our sample, the footpoints of MFRs carrying non-neutralized currents are co-spatial with strong-field regions ($|B| > 500$ G). More interestingly, high electric current densities concentrate on the PIL of the host active regions, manifested as two ribbons of opposite sign. Three typical events are shown in Figure 11. For these events, the identified feet are anchored at the far end of two current ribbons, as the three-dimensional flare-CME model (e.g. Janvier et al. 2014) predicted. However, the imbalance of R_z in two footpoints are found for most MFRs (Figure 9(a4)(b4)). For example, the 20110802 event, the R_z of FP+ is about 3.6, which is more than twice the R_z of FP- (about 1.6). In the following subsections, we further investigate asymmetric features inside the MFRs with non-neutralized current.

4.1. Asymmetric electric current distribution

The larger deviation of R_z is associated with asymmetric electric current distributions within two footpoints. Figure 12 shows two representative events, 20110930

and 20120614 events. For the 20110930 event, high current densities concentrate on the part of the sunspot, manifested as a spiral-like ribbon (see Figure 12 (a)). One foot of the MFR (FP-) covers the spiral-like current ribbon. But no obvious feature of electric current is found in the other foot (FP+). The R_z of FP- is as high as around 7.0, while the R_z of FP+ is only about 1.4. Similarly, a semiarc-like current ribbon is observed at the southeastern boundary of FP- in the 20120614 event (see Figure 12(b)). However, other footpoint of the MFR (FP+), which is anchored in the sunspot, carries relatively uniform current. The R_z of FP- is up to 6.5, while the R_z for FP+ is about 2.6.

More interestingly, for three events (20110930, 20120612 and 20140908), their leading footpoints are all co-spatial with the leading sunspots (see Figure 12). The value of R_z in these leading footpoints are higher than in the trailing footpoints (see bold font in the Table 2). Moreover, these three events are all associated with pre-eruption dimmings. For example, the 20140908 event, the R_z is about 3.4 in the leading footpoint, while the R_z is about 1.2 in the trailing one. On the contrary, for other four events (20110802, 20130812, 20131013 and 20150622), which are associated with post-eruption dimmings, the value of R_z in their trailing footpoints are higher than in the leading footpoints (see bold font in Table 3). For example, the 20110802 event, the R_z is about 3.6 in the trailing footpoint, while the R_z is about 1.6 in the leading one.

But the discrepancy is reduced when considering electric currents (I_z^{net} and I_z^{DC}) inside these MFRs. For most events, the values of I_z^{net} and I_z^{DC} for one foot are about 2 to 3 times than the other one. Furthermore, for the three events with pre-eruption dimmings (20110930, 20120614 and 20140908), the values of I_z^{DC} in the leading footpoints with very high R_z (up to 7.0) are smaller than in the trailing footpoints with relatively low R_z (around 1.2 to 2.6). For other two events with post-eruption dimmings (20110802 and 20131013), the values of I_z^{DC} in the trailing footpoints with higher R_z are larger than in the leading footpoints with lower R_z .

4.2. Asymmetric magnetic twist

For the MFRs carrying non-neutralized currents, both magnetic fluxes and direct currents in two footpoints are on the same order of magnitude and of opposite signs, in agreement with the scenario of current-carrying flux rope model. Therefore, we can further investigate their magnetic twist using three simple assumptions. Following our previous study (Wang et al. 2019), three different methods based on two assumptions, an axial symmetric cylindrical flux rope and nonlinear force-free magnetic configuration, are employed to estimate the average twist of MFRs. These methods were fully discussed in our previous study (Wang et al. 2019). In short, the average twist can be estimated by the following equations:

$$T = \frac{LB_\theta(r)}{2\pi r B_z(r)} \quad (Tw1)$$

$$T = \int_0^L \frac{\mu_0 J_{\parallel}}{4\pi B} dl \quad (Tw2)$$

where L is the length of the MFR axis, r is the distance to the axis. In this study, the geometric center of each foot is considered as the axis. L is estimated from the distance between centers of its feet, by assuming a circular-arc shape of the MFR. For the 8 MFRs with non-neutralized currents, the distance between conjugate feet varies from 26.7 Mm to 97.1 Mm, resulting in the length of MFRs ranging from 42.0 Mm to 152.5 Mm. For these two methods (Tw1 and Tw2), the twist per unit length τ at each foot is calculated from every pixel in FP+ and FP-. Then the average twist at each foot can be estimated as $\langle \tau \rangle L$. The uncertainties in the τ measurement, estimated from the error propagation, is very small compared with the standard deviation of τ at each foot. Therefore, we use the standard deviation of τ to estimate the uncertainty of the twist (δ_{Tw}) measurement.

Instead of measuring τ at each pixel and taking the average over all pixels, magnetic fluxes and electric currents in each foot can be directly used to calculate the average twist:

$$T = \frac{\mu_0 I}{4\pi\Phi} L \quad (Tw3)$$

The average twist calculated in this method will be very small when using I_z^{net} . In comparison, we also use the I_z^{DC} in each foot to estimate the average twist. These two different measurements are labeled as $Tw3_{net}$ and $Tw3_{DC}$, respectively. For this method, the uncertainty comes from δ_Φ and δ_I , which are estimated through error propagation.

The measurements from the above-mentioned three methods provide a possible range of twist in the MFRs. The results are shown in Table 4. For the first method, the average twist of the MFRs is around 1.0 to 3.0 turns before the eruption, close to the critical value for kink instability (Hood & Priest 1979; Török et al. 2004). In comparison, the twist calculated by the another two methods is smaller, around 0.5 to 2.5 turns. When considering I_z^{net} , the twist calculated from the third method will be very small, below 1.0 turn. Despite discrepancies in exact values, all three methods confirm that the average twist of these MFRs is around 1.0 turn before the eruption.

Similar to electric current distributions, the twist within two feet is not symmetric before the eruption. A direct comparison between magnetic twists of two footpoints is given in the Figure 13. We find low correlations between the average twists calculated in the two feet using the three different methods, the cross-correlation coefficient being 0.22 for Tw1, 0.39 for Tw2, 0.18 for $Tw3_{net}$ and 0.19 for $Tw3_{DC}$. The coefficient will be very low (0.06) for Tw1 when considering the leading/trailing footpoints. The average twist in one foot is about 1 to 2 times than in the other foot, especially for Tw2 and Tw3. The discrepancy becomes larger in $Tw3_{DC}$.

The first method shows that the average twist in the most leading footpoint is larger than in the trailing footpoint. For the MFRs with post-eruption dimmings, the results from the second and third methods also exhibit that the leading foot is associated with higher twist. But the opposite result is found in the MFRs with pre-eruptions dimmings when considering Tw2 and Tw3. For example, the 20110930 event, the

value of Tw2 in the trailing footpoint is around 1.9, which is more than twice in the leading footpoint.

Table 4. The average twist in the MFRs with non-neutralized current before eruptions

No.	Date	Distance (Mm)	Length (Mm)	Dimming label	FP Sign	Type	Tw1	Tw2	$Tw3_{net}$	$Tw3_{DC}$
4	20110802	64.8	101.7	<i>Post</i>	+	<i>T</i>	1.8 ± 0.6	1.5 ± 0.6	0.8 ± 0.1	1.2 ± 0.0
					-	<i>L</i>	2.6 ± 0.6	2.0 ± 0.7	0.6 ± 0.2	1.6 ± 0.1
5	20110930	26.7	42.0	<i>Pre</i>	+	<i>T</i>	1.8 ± 0.6	1.9 ± 0.7	0.3 ± 0.1	0.9 ± 0.1
					-	<i>L</i>	2.0 ± 0.7	0.8 ± 0.5	0.2 ± 0.0	0.3 ± 0.0
8	20120614	96.8	152.1	<i>Pre</i>	+	<i>L</i>	2.4 ± 0.6	0.7 ± 0.3	0.4 ± 0.1	0.6 ± 0.0
					-	<i>T</i>	1.6 ± 0.6	1.7 ± 0.7	1.0 ± 0.0	1.9 ± 0.0
13	20130812	53.0	83.3	<i>Post</i>	+	<i>L</i>	2.3 ± 0.6	1.8 ± 0.7	0.4 ± 0.2	1.0 ± 0.1
					-	<i>T</i>	1.6 ± 0.6	0.9 ± 0.6	0.2 ± 0.1	0.6 ± 0.1
16	20131013	47.9	75.3	<i>Post</i>	+	<i>L</i>	1.8 ± 0.6	1.7 ± 0.7	0.4 ± 0.3	1.0 ± 0.1
					-	<i>T</i>	1.4 ± 0.6	1.6 ± 0.6	0.7 ± 0.1	1.5 ± 0.1
21	20140825	58.3	91.5	<i>Pre</i>	+	<i>T</i>	1.7 ± 0.6	1.9 ± 0.7	0.8 ± 0.2	1.7 ± 0.1
					-	<i>L</i>	2.2 ± 0.5	1.5 ± 0.6	0.5 ± 0.2	1.1 ± 0.0
23	20140908	64.2	100.9	<i>Pre</i>	+	<i>L</i>	1.8 ± 0.5	1.0 ± 0.6	0.4 ± 0.0	0.5 ± 0.0
					-	<i>T</i>	1.1 ± 0.4	1.7 ± 0.7	0.1 ± 0.0	0.8 ± 0.0
27	20150622	97.1	152.5	<i>Post</i>	+	<i>T</i>	1.8 ± 0.6	1.8 ± 0.7	0.7 ± 0.1	1.5 ± 0.0
					-	<i>L</i>	1.4 ± 0.6	2.0 ± 0.7	0.4 ± 0.2	1.8 ± 0.1

NOTE— Table 4 shows the estimated value of magnetic twist from three methods (Tw1, Tw2, Tw3). The superscript '+'/'-' represent the twist calculated in the positive/negative footpoints respectively, and 'L/T' represent the twist calculated in the leading/trailing footpoints. The subscript 'net'/'DC' mean that we calculate Tw3 using I_z^{net} or I_z^{DC} . The errors for Tw1 and Tw2 are the standard deviation of τ , while the error for Tw3 comes from $\delta\Phi$ and δI .

5. SUMMARY & DISCUSSION

In this study, we investigate 28 eruptive events that exhibit obvious conjugate coronal dimmings. The AIA/SDO observations and HMI/SDO vector magnetograms are used to identify the footprints of erupting MFRs. Our results show two MFR categories, with or without significant net electric current. The two MFR populations have distinctive observational characteristics, implying different pre-eruptive magnetic field and evolution of these MFRs toward eruptions. In the following sections, we will first summarize what we have found and further compare our results with the existing flux-rope models.

Here we summarize what we have learned from our quantitative measurements of pre-eruptive magnetic properties of 28 erupting MFRs, whose feet are well identified by conjugate coronal dimmings:

1. In our sample, we find 9 events with pre-eruption conjugate dimmings, while the rest with post-eruption conjugate dimmings. All pre-eruption dimming events are accompanied by coronal structures considered to be plasma signatures of MFRs (e.g. sigmoids, filaments, expanding coronal structures). The pre-eruption dimmings evolve simultaneously with the MFR-like structures until they erupt as CMEs. Most post-eruption dimmings appear several minutes or dozens of minutes after the onset of flares.

2. Quantitative measurements of electric currents in 28 MFRs' conjugate feet show that only 8 of them carry significant non-neutralized currents ($R_z > 2.0$), that the rest might carry neutralized currents. The difference of magnetic flux and direct current between two MFR categories is not statistically significant (Figure 10).

3. The MFRs carrying non-neutralized currents exhibit the asymmetric electric current and magnetic twist at their feet. For most MFRs, electric currents (I_{net} and I_{DC}) in one foot are almost 2 to 4 times larger than the other one. For the average twist, the imbalance reduces to a factor of two. The R_z can be asymmetric, too, with non-neutralized current at one foot and neutralized current at the other. In particular, electric current may be concentrated in the form of a ribbon at one foot, but rather diffuse at the other (Figure 12).

5.1. *The pre-eruptive magnetic field: flux-rope models or others*

There has been a long-standing debate on the pre-eruptive magnetic field of erupting MFRs. In our study, combining evolution of pre-eruption dimmings and electric currents within dimming regions, we found signatures of different pre-eruptive magnetic fields. Different evolution of dimming fluxes are observed in the pre-eruption dimming events with or without net currents. For the pre-eruption dimming events with non-neutralized currents (see Figure 1(a)(d)), the dimming regions all undergo a rapidly expansion followed by quasi-static evolution stage before the eruption. The dimming fluxes will reach the maximum before the eruption. For example, in the 20120614 event, the expanding coronal structure observed by STEREO-B experi-

enced five-hours slow rising at speed of about 2 to 5 km s⁻¹ (see Figure 7) before the eruption. The expanding coronal structure finally evolved as a halo CME, which was identified as an MC (James et al. 2017) two days later when it passed through WIND spacecraft. Its footpoints as identified by pre-eruption dimmings carry non-neutralized currents ($R_z > 2.0$), implying a pre-existing current-carrying MFR. The pre-existing MFR was found by James et al. (2018) using NLFFF extrapolation (see Figure 3 in their paper). Therefore, we suggest that pre-eruption dimmings and non-neutralized currents are consistent with the pre-existing current-carrying MFR.

But for the rest pre-eruption dimming events with neutralized currents, the dimming regions experience a slow expansion followed by a stable stage (see Figure 1(b)(c)), which is similar to the evolution of some post-eruption dimmings. For these pre-eruption dimmings, the dimming fluxes start to rise before the eruption, but reach the maximum during the eruption. Zhou et al. (2017) had studied the 20110621 event in detail. A pre-eruption sigmoidal structure was observed in the EUV hot channel and shared the same location with a filament (see Figure 2 in their paper). The conjugate dimmings detected in our study are located in the two ends of the filament-sigmoid structure. The R_z within the two identified footpoints are around 1.0, implying a neutralized flux-rope model.

The situation is more complicated for the post-eruption dimming events. Only 4 of 19 post-eruption dimming events carry non-neutralized currents (Table 3). For these four events, high electric current densities of different sign distribute on the two sides of the PIL and their identified footpoints anchor at two ends of current ribbons (see Figure 11), conforming to the 3D extension of standard flare model (Janvier et al. 2014). For example, for the 20130812 event, Liu et al. (2016) had investigated the host active region 11817 during 2013 August 10 to 12. Aided by NLFFF method, they identified a Double-decker MFR system one day before the 20130812 event. Awasthi et al. (2018) also applied the NLFFF extrapolation method to the 20150622 event and found a pre-existing multi-flux-rope system (see the Figure 1 in their paper). These studies further suggest that the post-eruption dimmings with non-neutralized currents may be also associated with pre-existing MFRs. But for the other post-eruption dimming events, the evolution of dimmings reflect the formation process of erupting MFRs. The onset of the dimming typically lags the onset of the flare by several minutes or even several tens of minutes. Wang et al. (2017) had investigated the 20151104 event and found that the main body of a highly twisted MFR was formed during the eruption via magnetic reconnection, which was associated with the development of dimmings inside a pair of closed hooked ribbons.

5.2. *The role of magnetic reconnection in the dynamic evolution of conjugate dimmings*

For both pre-eruption and post-eruption dimming events, both flare ribbons and dimmings are dynamically evolving, as a result, the accumulative ribbons and dim-

ming regions overlap each other (see Figure 3 and Figure 4). For pre-eruption dimmings, flare ribbons will erode part of dimming areas. For the 20110930 and 20120614 event, more than half of dimming areas disappear after the flares (see Figure 8 (a) and (d)). The dimming areas can also extend in area after the flare, e.g. the 20130830 event (Figure 8 (b)), or be almost unchanged after the flare, e.g. the 20110621 event (Figure 8 (c)). The loss of pre-eruption dimming areas may reflect internal changes of the pre-existing MFRs, suggesting that the pre-existing MFRs may undergo internal reconnections due to the presence of QSLs inside the rope (e.g., Awasthi et al. 2018), which are termed 'rr-rf' reconnections in Aulanier & Dudík (2019), with 'r' referring to the rope field and 'f' to post-flare loops. For most post-eruption dimming events, dimming regions are partially swept by flare ribbons (see Figure 4), implying MFRs may be built up via reconnection during the eruptions. The complexity of the role of 3D reconnection in buildup of MFRs requires further investigation beyond the scope of this study.

In our sample, morphological evolution of both pre-eruption and post-eruption dimmings are relatively stable. But we also find several events with rapid drifting dimmings, for example, the 20120712 event. This event was also well investigated by many previous studies (e.g. Dudík et al. 2014; Cheng et al. 2014; Cheng & Ding 2016). Apparent slipping motions of both flare and erupting loops were observed in this event (see Figure 6,8,10 in Dudík et al. 2014). Dudík et al. (2014) further indicated that the slipping motions fed the MFR with twisted field lines surrounding its core, leading to the MFR expansion. As a result, the dimmings drift following the slipping motions. The drifting of dimmings may reflect the drifting of the MFR footpoints. Aulanier & Dudík (2019) indicated that a series of coronal reconnections can change the foot-point area of flux rope. They also suggested two new reconnection terminologies: aa-rf and ar-rf reconnections (see Figure 4, Figure 5, and Figure 6 in their paper), with 'a' referring to the arcade field. Distinctive morphological evolution of conjugate dimmings may suggest different processes of reconnection.

5.3. *The non-neutralized current inside the MFR*

Identification of the MFR's feet is very challenging. Our method outlines possible areas of footpoints by detecting conjugate coronal dimmings. It is important to keep in mind that conjugate dimmings can map the footpoints of erupting MFRs but may not cover the whole region of the footpoints. On the other hand, our results are subject to the accuracy of identification, which has been explained in Appendix A.

Distinctive distributions of electric current at the MFR feet may imply different internal structures of flux-ropes. For the MFRs with non-neutralized currents, high electric current densities can concentrate on the center of the footpoint (e.g. the 20130812 event), or the boundary of the footpoint (e.g. the 20131012 event). Furthermore, high electric current densities can develop into smooth continuous ribbons, e.g a spiral-like ribbon (the 20110930 event) and a semiarc-like ribbon (the 20120614

event). But it is hard to tell the distribution of electric current within the MFRs with neutralized currents, when opposite signs of current densities are mixed and randomly distributed. In our sample, most footpoints associated with neutralized currents are located in the relatively weak field. The main problem here is uncertainties of vertical electric current, especially in the weak field, due to large uncertainties of transverse field. It is important to keep in mind that our results only give a rough estimate of the degree of current neutralization of these MFRs. Instruments with higher resolution and sensitivity (e.g. the Daniel K. Inouye Solar Telescope) are required to reveal more detailed current distributions within the MFRs.

Previous numerical simulations indicated that photospheric flows may play a significant role in the development of net current in the solar active regions (e.g. Török et al. 2014; Dalmasse et al. 2015). In the MHD simulation of Török et al. (2014), the buildup of net current inside the MFR occurred when strong shear developed along the PIL. Indeed, shear flows at speed of 1 km s^{-1} are observed along the PILs for the three events in Figure 11. Particularly, for the 20120614 event, the semiarc-like current ribbon observed in the FP- (Figure 12 (b)) shares the same location with shear flows. A parametric MHD simulation from Dalmasse et al. (2015) also confirmed that both shear motions and twisting motions below the MFR could inject net current into its feet. Similarly, for the 20110930 event, a spiral-like current ribbon is observed in the footpoint of the MFR, which is co-spatial with the rotational sunspot (Figure 12 (a)). Different from their simulations, however, the observed twisting motion only occurs in one foot of the studied MFR, which may explain the asymmetric electric current and magnetic twist distribution. More evidences are required to verify the origin of net currents.

In conclusion, we investigate pre-eruptive magnetic properties at footpoints of 28 MFRs using HMI vector magnetogram. Our statistical study indicates that about 28% (8 out of 28) of the MFRs carry significant non-neutralized currents ($R_z > 2.0$) and half of them are associated with pre-eruption dimmings at the footpoints, suggesting that such MFRs are most likely formed prior to eruption. The distributions of electric current and magnetic twist at the MFR footpoints as well as the asymmetry of the distributions may help us to diagnose the internal structures of the MFRs and to further may shed light on their formation mechanism.

We thank two unknown referees for very helpful comments. This work was supported by National Natural Science Foundation of China (NSFC 12003032, 11925302, 4218810), the China Postdoctoral Science Foundation (Grant No. 2019TQ0313), the Strategic Priority Program of the Chinese Academy of Sciences (XDB41000000), and the Fundamental Research Funds for the Central Universities.

REFERENCES

- Aulanier, G., & Dudík, J. 2019, *A&A*, 621, A72,
doi: [10.1051/0004-6361/201834221](https://doi.org/10.1051/0004-6361/201834221)
- Avallone, E. A., & Sun, X. 2020, *ApJ*, 893, 123,
doi: [10.3847/1538-4357/ab7afa](https://doi.org/10.3847/1538-4357/ab7afa)
- Awasthi, A. K., Liu, R., Wang, H., Wang, Y., & Shen, C. 2018, *ApJ*, 857, 124,
doi: [10.3847/1538-4357/aab7fb](https://doi.org/10.3847/1538-4357/aab7fb)
- Barczynski, K., Aulanier, G., Janvier, M., Schmieder, B., & Masson, S. 2020, *ApJ*, 895, 18, doi: [10.3847/1538-4357/ab893d](https://doi.org/10.3847/1538-4357/ab893d)
- Bobra, M. G., Sun, X., Hoeksema, J. T., et al. 2014, *Solar Physics*, 289, 3549
- Cheng, J., & Qiu, J. 2016, *The Astrophysical Journal*, 825, 37
- Cheng, X., & Ding, M. 2016, *The Astrophysical Journal Supplement Series*, 225, 16
- Cheng, X., Ding, M. D., Zhang, J., et al. 2014, *ApJ*, 789, 93,
doi: [10.1088/0004-637X/789/2/93](https://doi.org/10.1088/0004-637X/789/2/93)
- Cheung, M. C. M., & Isobe, H. 2014, *Living Reviews in Solar Physics*, 11, 3,
doi: [10.12942/lrsp-2014-3](https://doi.org/10.12942/lrsp-2014-3)
- Dalmasse, K., Aulanier, G., Démoulin, P., et al. 2015, *ApJ*
- Démoulin, P., & Aulanier, G. 2010, *ApJ*, 718, 1388,
doi: [10.1088/0004-637X/718/2/1388](https://doi.org/10.1088/0004-637X/718/2/1388)
- Dissauer, K., Veronig, A. M., Temmer, M., & Podladchikova, T. 2019, *ApJ*, 874, 123,
doi: [10.3847/1538-4357/ab0962](https://doi.org/10.3847/1538-4357/ab0962)
- Dissauer, K., Veronig, A. M., Temmer, M., Podladchikova, T., & Vanninathan, K. 2018a, *ApJ*, 855, 137,
doi: [10.3847/1538-4357/aaadb5](https://doi.org/10.3847/1538-4357/aaadb5)
- . 2018b, *ApJ*, 863, 169,
doi: [10.3847/1538-4357/aad3c6](https://doi.org/10.3847/1538-4357/aad3c6)
- Dudík, J., Janvier, M., Aulanier, G., et al. 2014, *ApJ*, 784, 144,
doi: [10.1088/0004-637X/784/2/144](https://doi.org/10.1088/0004-637X/784/2/144)
- Fan, Y. 2009, *The Astrophysical Journal*, 697, 1529
- Fan, Y., & Gibson, S. 2004, *The Astrophysical Journal*, 609, 1123
- Georgoulis, M. K., Titov, V. S., & Mikić, Z. 2012, *ApJ*, 761, 61,
doi: [10.1088/0004-637X/761/1/61](https://doi.org/10.1088/0004-637X/761/1/61)
- Gosling, J. T. 1990, *Physics of magnetic flux ropes*, 343
- Harra, L. K., Hara, H., Imada, S., et al. 2007, *Publications of the Astronomical Society of Japan*, 59, S801
- Harra, L. K., & Sterling, A. C. 2001, *The Astrophysical Journal Letters*, 561, L215
- Harrison, R., & Lyons, M. 2000, *Astronomy and Astrophysics*, 358, 1097
- Harvey, K. L., & Recely, F. 2002, *Solar Physics*, 211, 31
- Hoeksema, J. T., Liu, Y., Hayashi, K., et al. 2014, *Solar Physics*, 289, 3483
- Hood, A. W., & Priest, E. 1979, *Solar Physics*, 64, 303
- Hu, Q., Qiu, J., Dasgupta, B., Khare, A., & Webb, G. 2014, *The Astrophysical Journal*, 793, 53
- James, A., Green, L., Palmerio, E., et al. 2017, *Solar Physics*, 292, 71
- James, A. W., Valori, G., Green, L. M., et al. 2018, *ApJL*, 855, L16,
doi: [10.3847/2041-8213/aab15d](https://doi.org/10.3847/2041-8213/aab15d)
- Janvier, M., Aulanier, G., Bommier, V., et al. 2014, *ApJ*, 788, 60,
doi: [10.1088/0004-637X/788/1/60](https://doi.org/10.1088/0004-637X/788/1/60)
- Kaiser, M. L., Kucera, T., Davila, J., et al. 2008, *Space Science Reviews*, 136, 5
- Kazachenko, M. D., Lynch, B. J., Welsch, B. T., & Sun, X. 2017, *ApJ*, 845, 49,
doi: [10.3847/1538-4357/aa7ed6](https://doi.org/10.3847/1538-4357/aa7ed6)
- Kontogiannis, I., Georgoulis, M. K., Guerra, J. A., Park, S.-H., & Bloomfield, D. S. 2019, *SoPh*, 294, 130,
doi: [10.1007/s11207-019-1523-6](https://doi.org/10.1007/s11207-019-1523-6)
- Leka, K. D., Barnes, G., Crouch, A. D., et al. 2009, *SoPh*, 260, 83,
doi: [10.1007/s11207-009-9440-8](https://doi.org/10.1007/s11207-009-9440-8)
- Leka, K. D., Canfield, R. C., McClymont, A. N., & van Driel-Gesztelyi, L. 1996, *ApJ*, 462, 547, doi: [10.1086/177171](https://doi.org/10.1086/177171)
- Lemen, J. R., Akin, D. J., Boerner, P. F., et al. 2012, *Solar physics*, 275, 17
- Liu, R., Kliem, B., Titov, V. S., et al. 2016, *The Astrophysical Journal*, 818, 148

- Liu, Y., Sun, X., Török, T., Titov, V. S., & Leake, J. E. 2017, *The Astrophysical Journal Letters*, 846, L6
- Longcope, D. W., & Beveridge, C. 2007, *ApJ*, 669, 621, doi: [10.1086/521521](https://doi.org/10.1086/521521)
- Longcope, D. W., & Welsch, B. T. 2000, *ApJ*, 545, 1089, doi: [10.1086/317846](https://doi.org/10.1086/317846)
- Melrose, D. B. 1991, *ApJ*, 381, 306, doi: [10.1086/170652](https://doi.org/10.1086/170652)
- . 1995, *ApJ*, 451, 391, doi: [10.1086/176228](https://doi.org/10.1086/176228)
- Metcalf, T. R. 1994, *SoPh*, 155, 235, doi: [10.1007/BF00680593](https://doi.org/10.1007/BF00680593)
- Metcalf, T. R., Leka, K. D., Barnes, G., et al. 2006, *SoPh*, 237, 267, doi: [10.1007/s11207-006-0170-x](https://doi.org/10.1007/s11207-006-0170-x)
- Moore, R. L., Sterling, A. C., Hudson, H. S., & Lemen, J. R. 2001, *The Astrophysical Journal*, 552, 833
- Parker, E. N. 1996, *ApJ*, 471, 485, doi: [10.1086/177983](https://doi.org/10.1086/177983)
- Pesnell, W. D., Thompson, B. J., & Chamberlin, P. 2011, in *The Solar Dynamics Observatory* (Springer), 3–15
- Qiu, J., & Cheng, J. 2017, *The Astrophysical Journal Letters*, 838, L6
- Qiu, J., Hu, Q., Howard, T. A., & Yurchyshyn, V. B. 2007, *The Astrophysical Journal*, 659, 758
- Scholl, I. F., & Habbal, S. R. 2008, *Solar Physics*, 248, 425
- Sun, X., & Cheung, M. C. M. 2020, *Solar physics*
- Titov, V., & Démoulin, P. 1999, *Astronomy and Astrophysics*, 351, 707
- Török, T., Kliem, B., & Titov, V. 2004, *Astronomy & Astrophysics*, 413, L27
- Török, T., Leake, J. E., Titov, V. S., et al. 2014, *ApJL*, 782, L10, doi: [10.1088/2041-8205/782/1/L10](https://doi.org/10.1088/2041-8205/782/1/L10)
- Vemareddy, P. 2019, *MNRAS*, 486, 4936, doi: [10.1093/mnras/stz1020](https://doi.org/10.1093/mnras/stz1020)
- Wang, W., Liu, R., Wang, Y., et al. 2017, *Nature communications*, 8, 1330
- Wang, W., Zhu, C., Qiu, J., et al. 2019, *The Astrophysical Journal*, 871, 25
- Webb, D., Cliver, E., Crooker, N., St Cyr, O., & Thompson, B. 2000, *Journal of Geophysical Research: Space Physics*, 105, 7491
- Xing, C., Cheng, X., & Ding, M. D. 2020, *The Innovation*, 1, 100059, doi: [10.1016/j.xinn.2020.100059](https://doi.org/10.1016/j.xinn.2020.100059)
- Zhou, Z., Zhang, J., Wang, Y., Liu, R., & Chintzoglou, G. 2017, *ApJ*, 851, 133, doi: [10.3847/1538-4357/aa9bd9](https://doi.org/10.3847/1538-4357/aa9bd9)

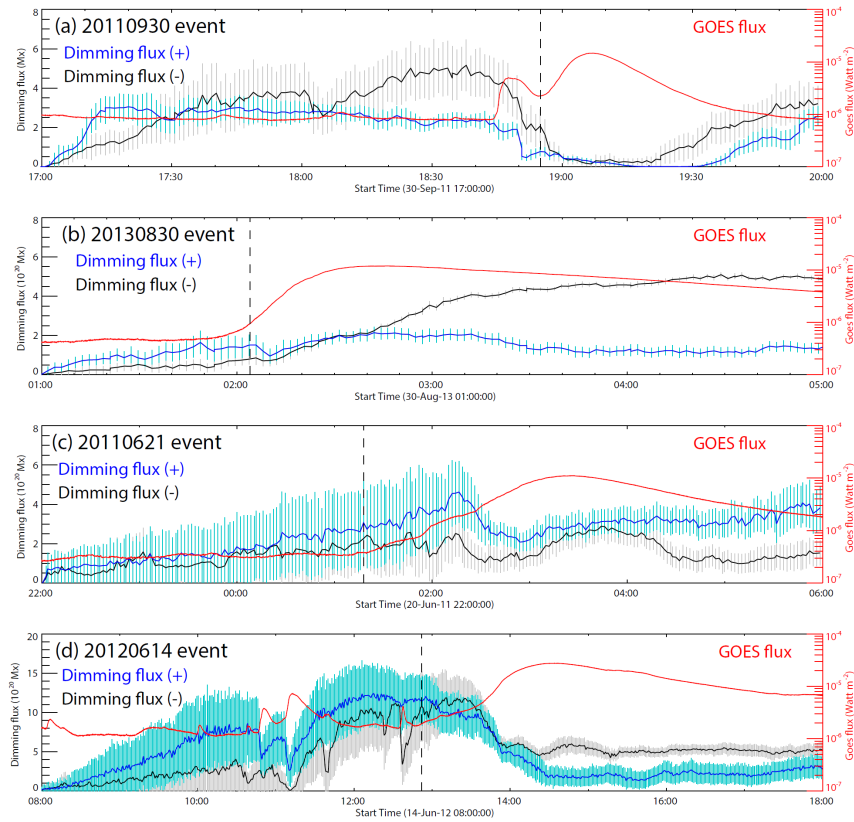


Figure 1. Evolution of pre-eruption coronal dimmings for four events. All diagrams show temporal evolution of dimming fluxes (black for negative, blue for positive) and GOES flux (red). The vertical dashed line represents the onset of the flare for each event.

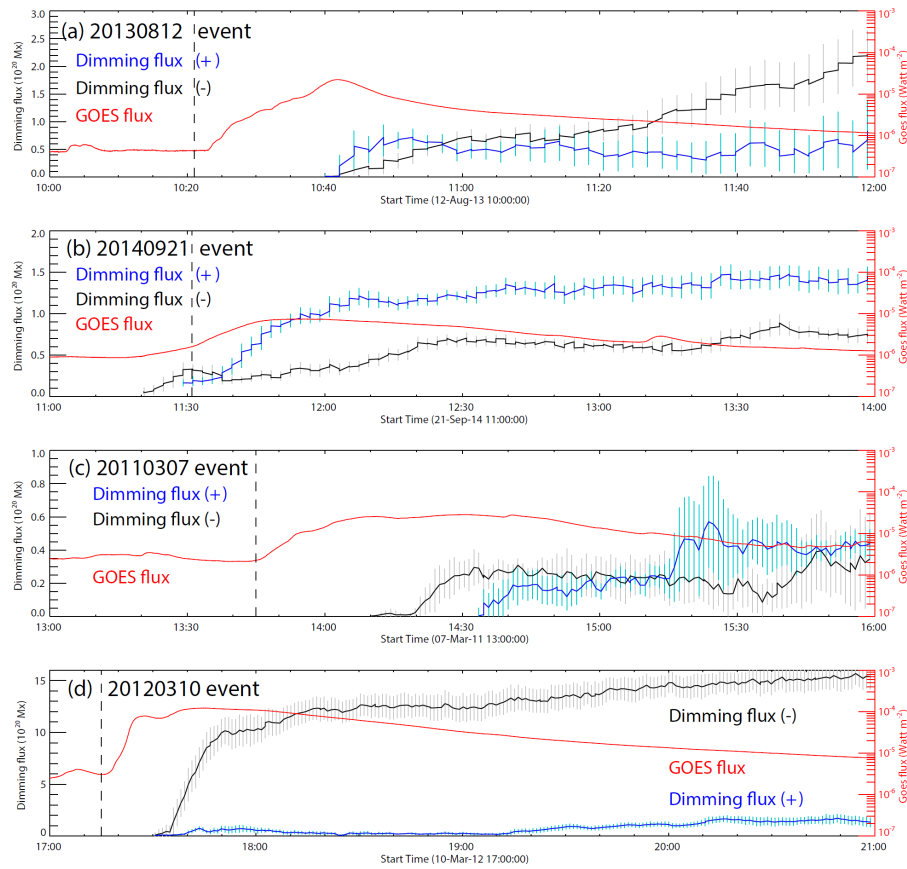


Figure 2. Evolution of post-eruption coronal dimmings for four events. All diagrams show temporal evolution of dimming fluxes (black for negative, blue for positive) and GOES flux (red). The vertical dashed line represents the onset of the flare for each event.

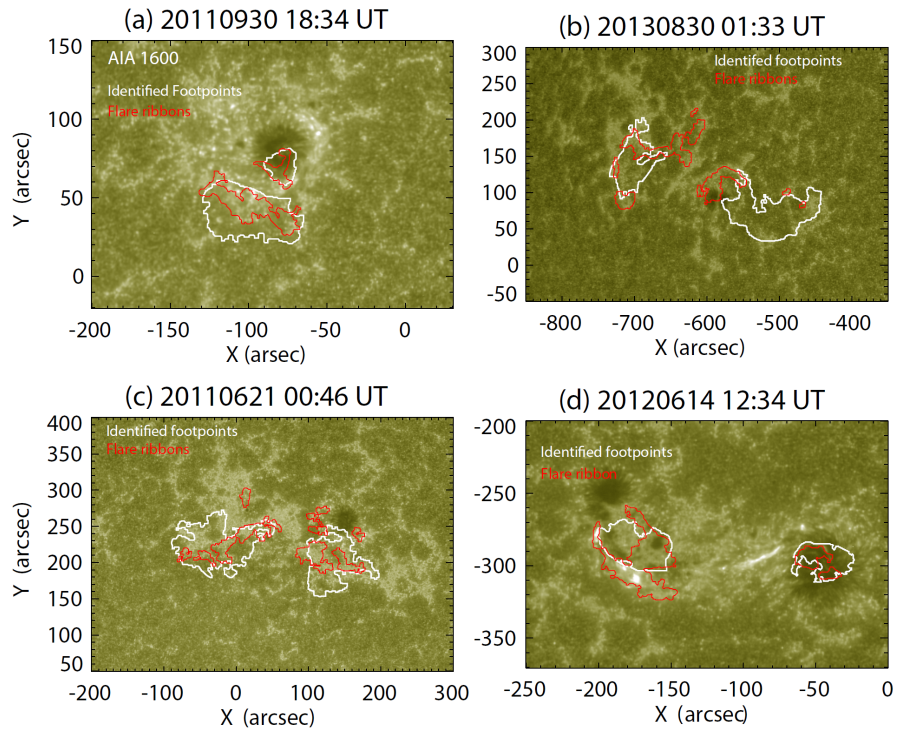


Figure 3. Pre-eruption dimming events: relative locations between identified footpoints and flare ribbons. All snapshots are from AIA 1600 channel. For each event, two contours show identified footpoints from conjugate dimmings (white) and detected flare ribbons (red).

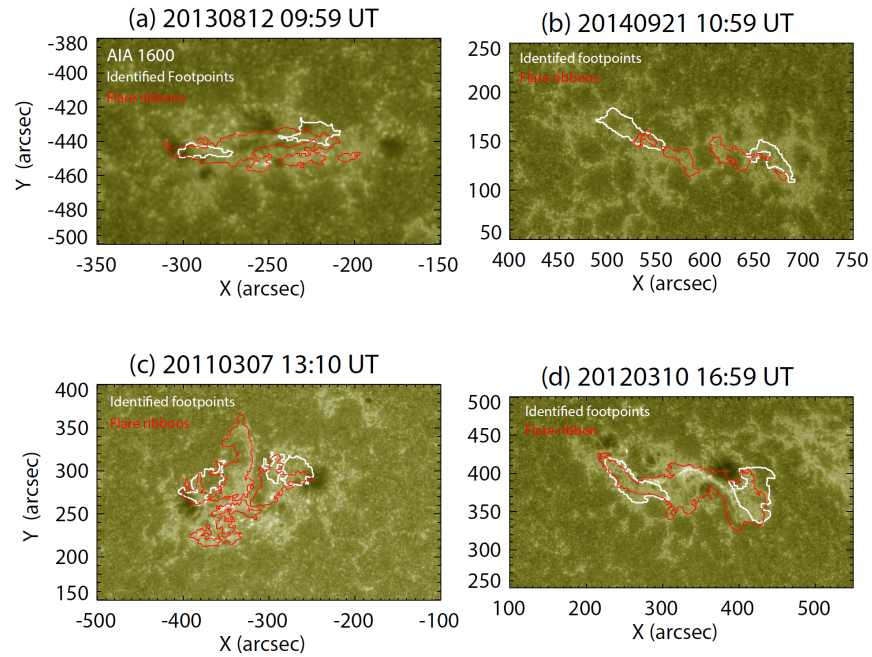


Figure 4. Post-eruption dimming events: relative locations between identified footpoints and flare ribbons. All snapshots are from AIA 1600 channel. For each event, two contours show identified footpoints from conjugate dimmings (white) and detected flare ribbons (red).

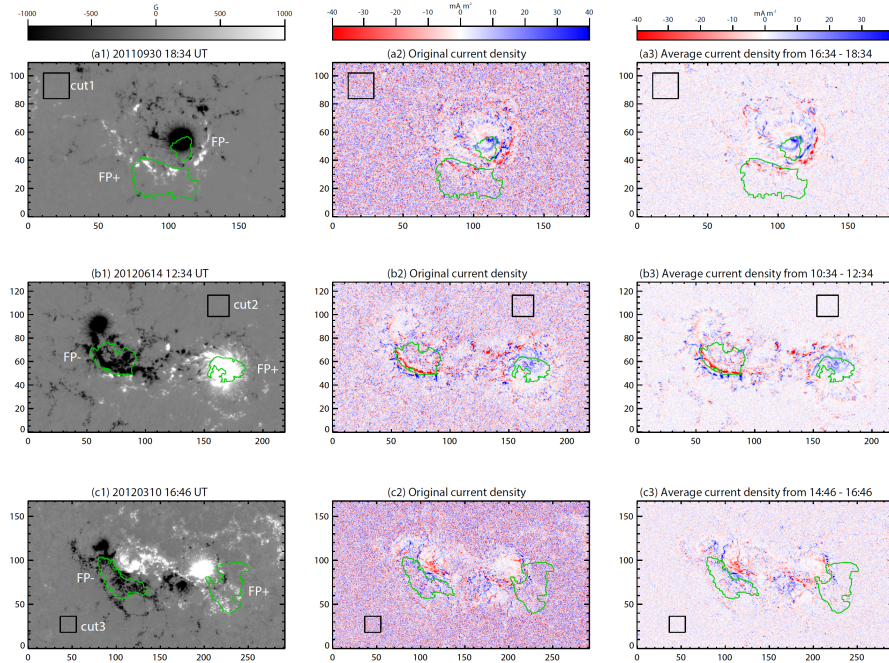


Figure 5. Examples for HMI vector magnetogram (left), original current density maps (center) and timing-averaged current density maps (right). Four rows represent four different events respectively. Green contours show the identified footpoint regions.

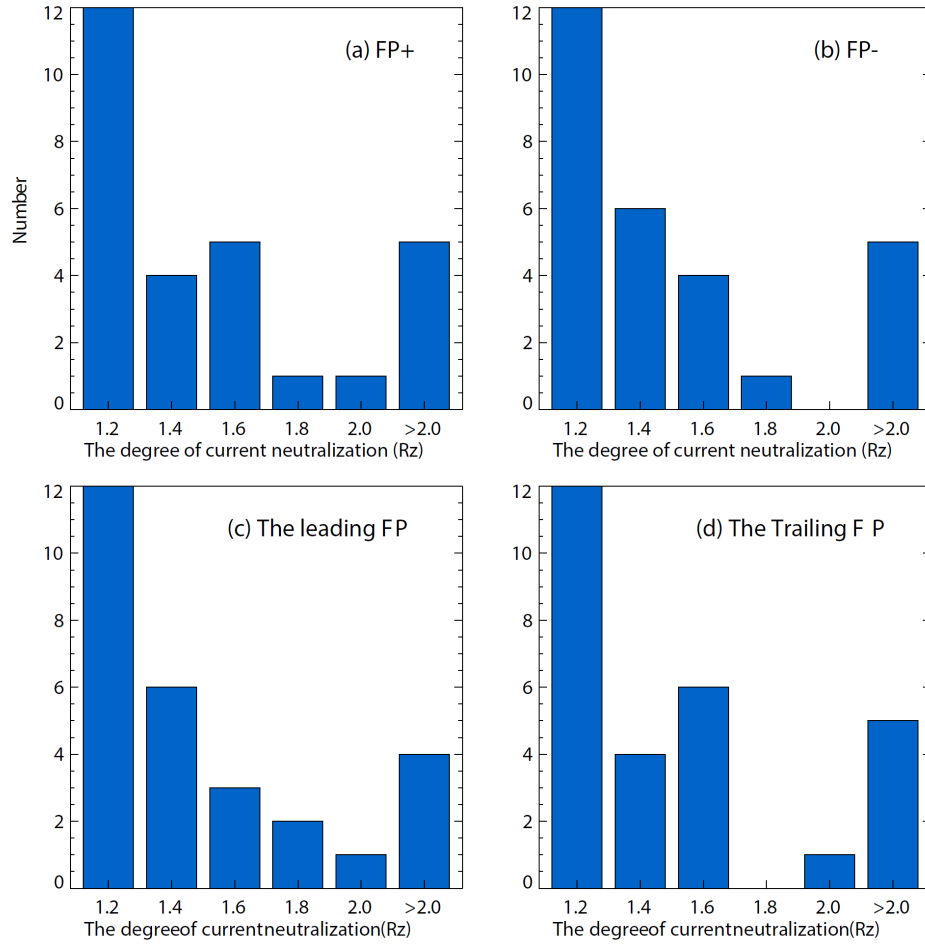


Figure 6. The histogram of degree of current neutralization R_z . (a) shows the R_z estimated in FP+, and (b) shows the R_z for FP-. (c) shows the R_z in the leading FP, and (d) shows the R_z in the trailing FP.

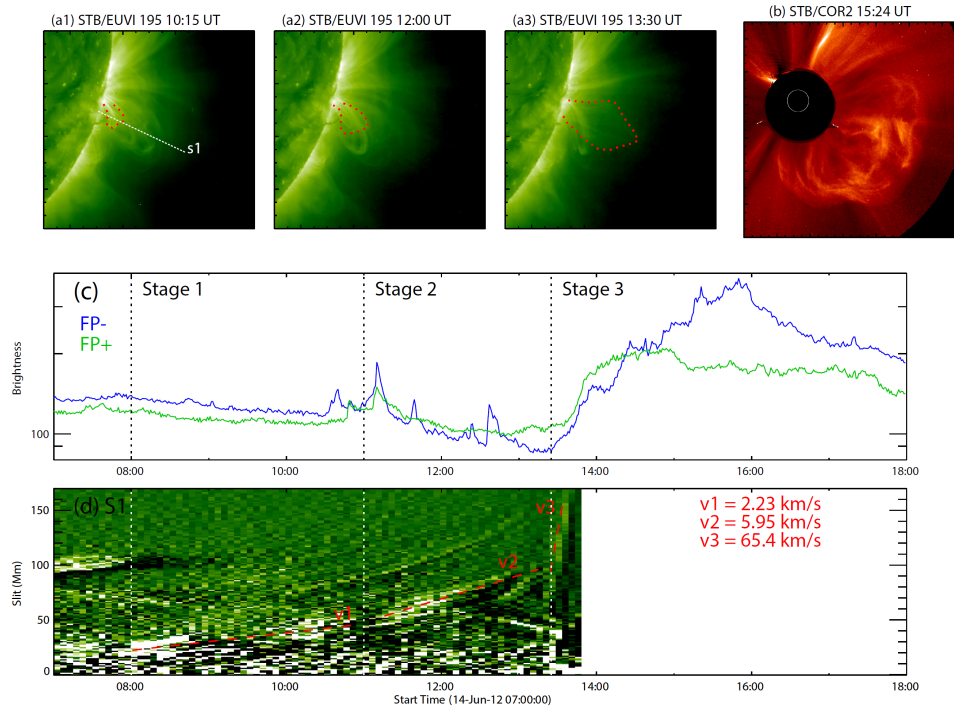


Figure 7. One typical case of pre-eruption dimmings: the 20120614 event. The panels (a1) to (a3) show the expanding coronal structure observed in 195 passband by STEREO-B/EUVI, which finally evolved as a halo CME captured by STEREO-B/COR2 (b). The diagram (c) shows the temporal profiles of brightness in AIA 304. Green and blue curves represent the average brightness in two identified footpoints (see white contours in the Figure 3 (d)). The diagram (d) represents the time–distance map along “s1” in (a1). Three linear fittings are indicated by red dashed lines. Three vertical dashed lines mark the beginning of three different stages. More detailed information can be found in the Wang et al. (2019).

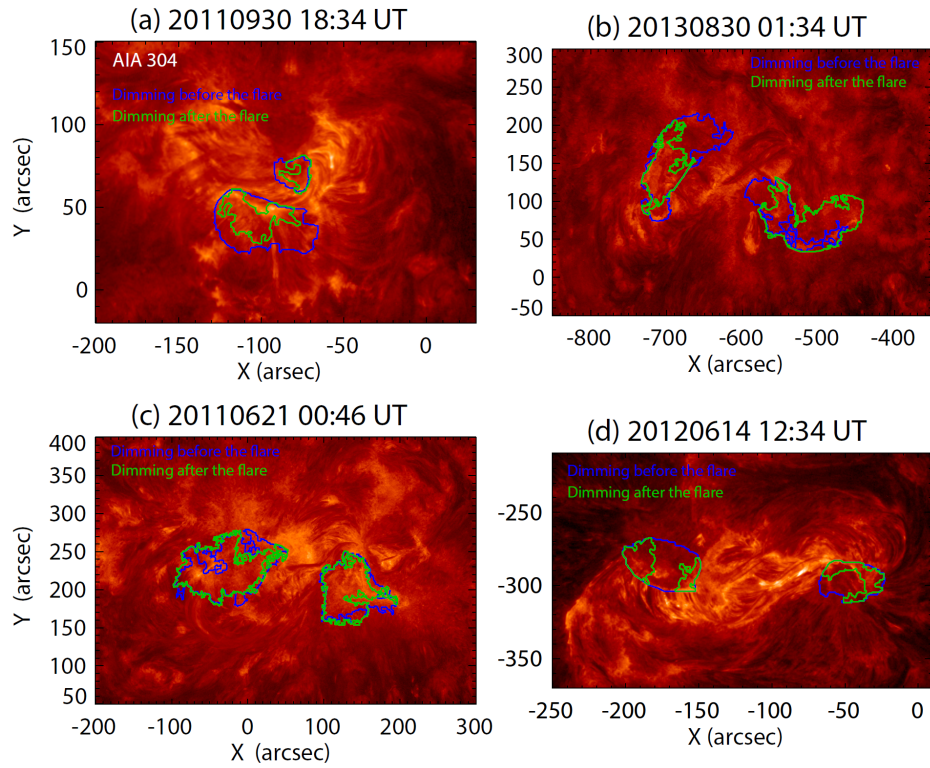


Figure 8. The observational feature of pre-eruption dimmings. All snapshots are from AIA 304 channel. For each event, two contours show the dimming regions appear before (blue) or after (green) the onset of the flare.

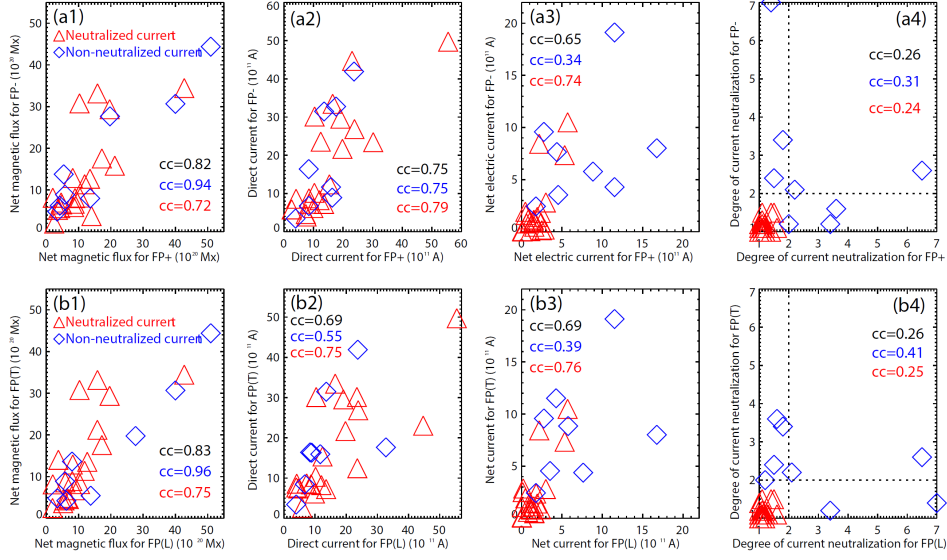


Figure 9. The correlation between magnetic properties measured in conjugate footpoints of studied MFRs. We compare net magnetic fluxes, direct electric currents, net electric currents and the degree of current neutralization for two footpoints. The red triangle is for the MFRs with neutralized current, while the blue rhombus is for the MFRs with non-neutralized current. The 'FP+/-' present the FP with positive/negative magnetic field, while the 'FP(L/T)' stand for the leading/trailing FP. The 'cc' is the absolute value of the cross correlation coefficient.

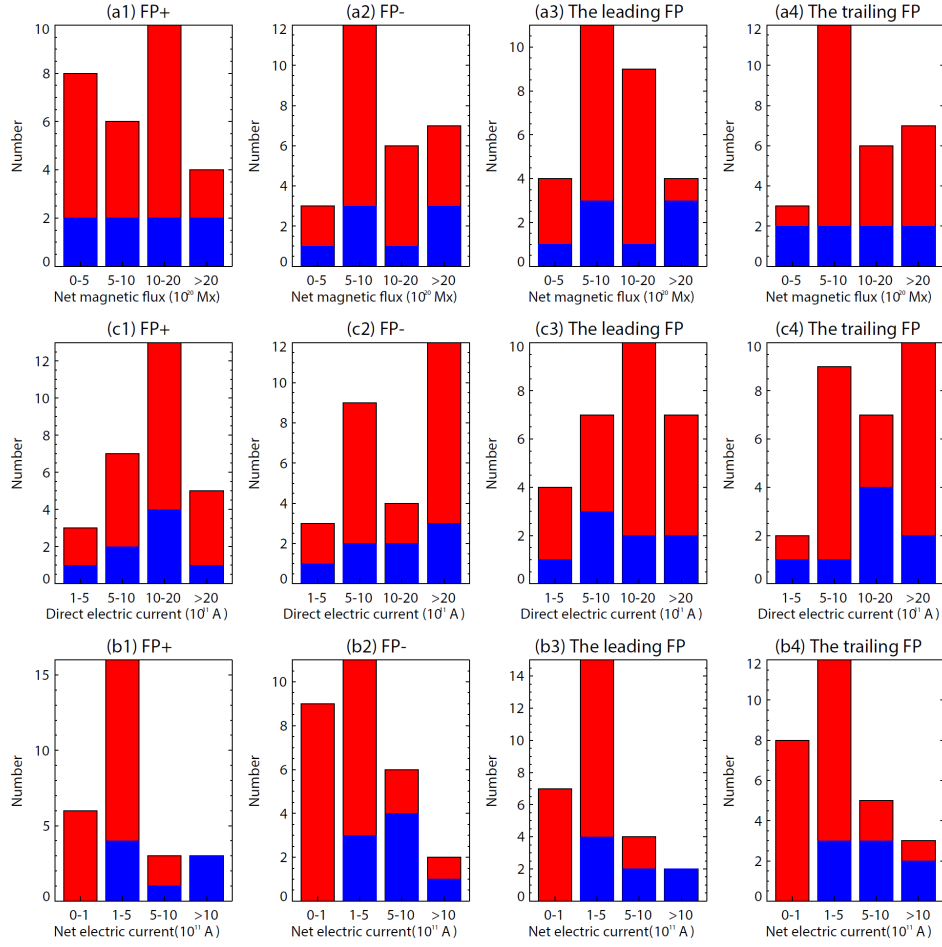


Figure 10. Comparison between properties of the MFRs with or without net currents. Red part represents the number distribution of the MFR with neutralized current, while blue part represents the other one.

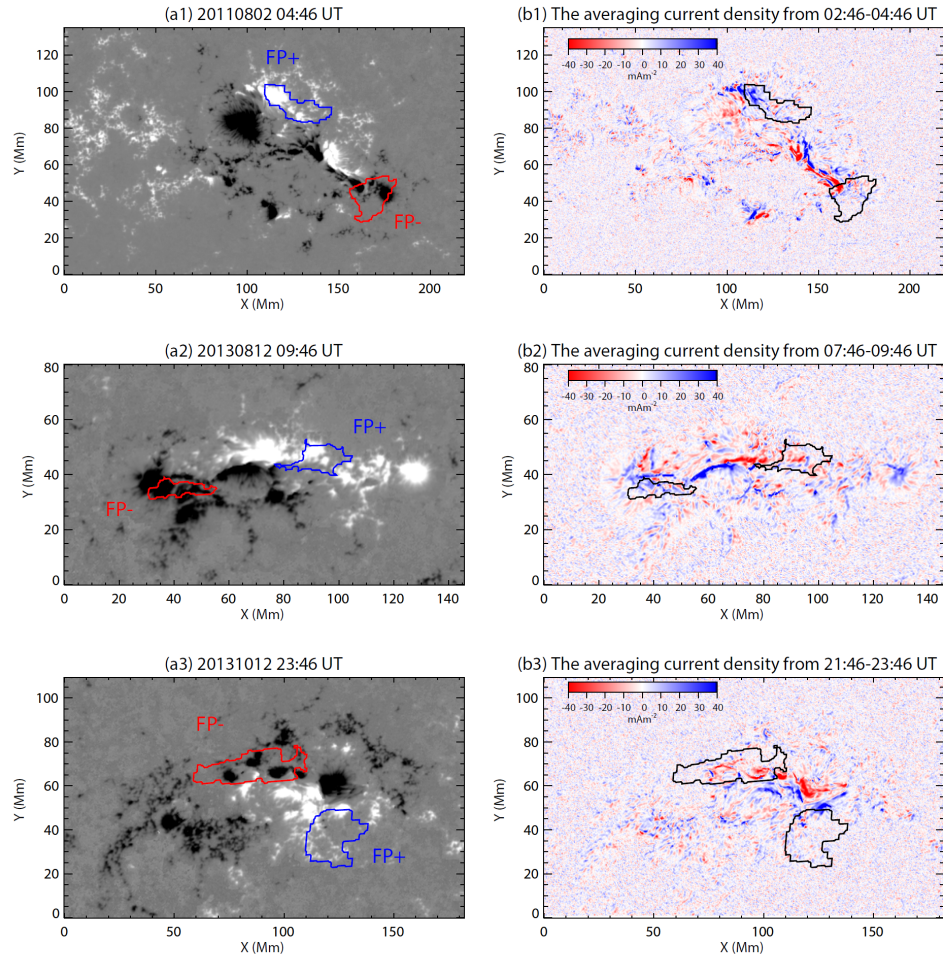


Figure 11. Three typical post-eruption dimmings with non-neutralized currents. The panels in the left are vertical magnetic field from HMI vector magnetogram. The panels in the right are the time-averaging current density maps. Two contours in each panel show the identified footpoint regions.

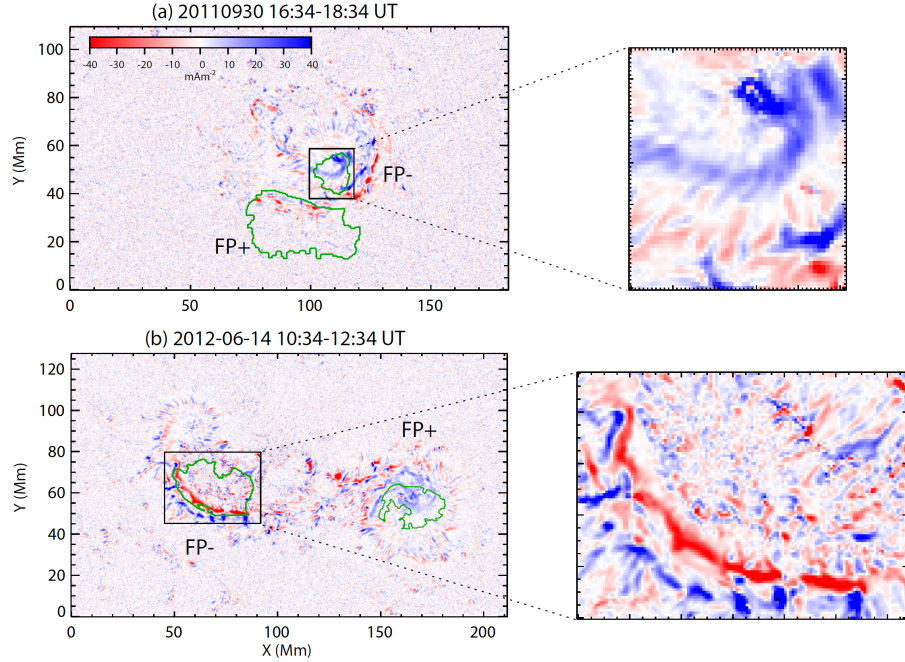


Figure 12. Asymmetric current distribution in the two feet of the MFRs. (a) and (b) are two snapshots of vertical current density maps for the 20110930 and 20120614 events. Two green contours in each panel represent the footpoints.

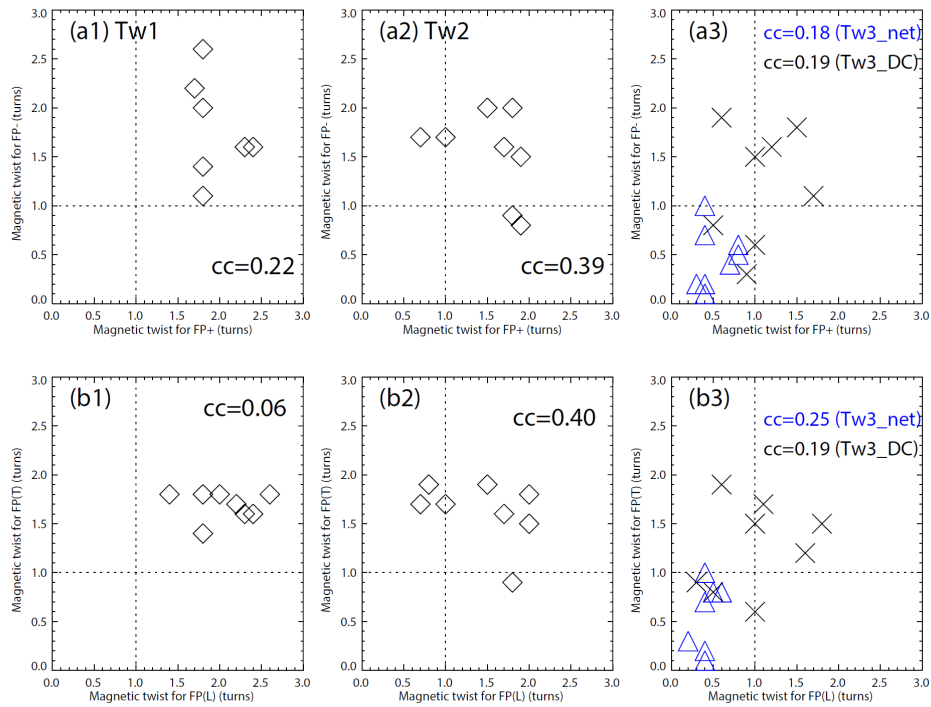


Figure 13. Comparison between magnetic twist in two footpoints of the MFRs with non-neutralized currents. Three columns show the average twist for three methods (Tw1, Tw2, Tw3) in two footpoints respectively. For the (a3) and (b3), the blue triangle is for $Tw3_{net}$, while the dark cross is for $Tw3_{DC}$. A critical value of magnetic twist (1.0 turn) are marked as two dashed lines in three panels.

APPENDIX

A. IDENTIFYING CONJUGATE DIMMINGS AND ASSOCIATED UNCERTAINTIES

Our previous studies (Wang et al. 2017, 2019) had employed image thresholding segmentation methods to detect coronal dimmings. In short, the method would count all the pixels when their brightness are reduced by around 20% to 40% compared with their original value in the active region. However, morphological characteristics of coronal dimmings are complex, manifesting as multiple fragment-like areas or some large extended areas. The main problem is how to distinguish MFR feet-related dimmings from other type of dimmings. Previous studies (e.g. Dissauer et al. 2018b) considered so-called core dimmings as the feet-related dimmings. But the core dimmings were always shown as small fragments (see Figure 2 in the Dissauer et al. (2018b)), even occurred at different locations. Inspired by 3D extension of flare/CME models (e.g. Moore et al. 2001; Longcope & Beveridge 2007; Janvier et al. 2014), for two-ribbon flares, feet-related dimmings should be co-spatial with flare ribbons. Wang et al. (2017) then took two closed hooks as boundaries of feet-related dimmings and finally attained two well identified footpoints of the MFR. Two studies (Qiu & Cheng 2017; Wang et al. 2019) further confirmed that a pair of conjugate dimmings, which occur in the vicinity of flare ribbons and are associated with two opposite signs of magnetic polarities, map two footpoints of MFRs.

In this study, a series of steps mentioned in the Section 2.2 are used to seek two boundaries of conjugate dimmings automatically. Initially, for each event, our method will automatic check all images from the whole observational time and output two areas as the candidate conjugate dimming regions. Analyzing all EUV channels during several hours for each event will cost a lot of time. To minimize the amount of computation, we only check morphology of dimmings at several moments (e.g. before the eruption, the onset of flare, after the eruption) due to relatively slow evolution of dimming regions. In the following steps, all detected regions will be projected into the HMI vector magnetogram. The regions with mixed polarities will be deleted. Then we compare the location of flare ribbons and the detected dimming regions. After this processing, for most events, the remaining dimming regions will distribute mainly in two areas. But if the remaining dimming regions distribute in many different positions, we will further check magnetic connectivity of these positions via NLFFF models to further select two possible areas. In this study, only several events are required to check magnetic connectivity. Then the method will track the dimmings in AIA 304 channel at a cadence of 2 minutes starting from two hours before the eruption within two boundaries from previous steps. As explained in the Section 2.2, two type of dimmings, pre-eruption and post-eruption, are observed in our study. For the pre-eruption dimmings, the method will keep going back in time to seek the onset

of dimmings. By employing a trial-and-error approach, we find that the threshold of pre-eruption dimmings are around 15% to 30%. Similarly, we also recheck the evolution of post-eruption dimmings and find their threshold of around 30% to 50%. Figure 2 shows examples of dimming evolution.

The tracking of 28 events further show that the movement of dimmings is relatively complicated. As discussed in the Section 5.2, different dynamic evolution of dimmings are largely associated with the magnetic reconnection between the enveloped field and the MFR itself. Then the dimmed pixels only appear at the stage of rapid change are removing from our detection. We recheck the bright-curve of all detected pixels during the whole observational time. The flagged pixels with the brightness continues to drop at least 10 minutes are selected. Finally, we outline two regions, including all survived pixels, as two fixed regions.

It is very difficult to provide the uncertainties of identified footpoint regions. As mentioned above, a series of steps are employed to outline the footpoint regions. The errors of detected dimmings can be quantified by varying the threshold $\pm 10\%$ (see the errors in the Figure 2). But locations and quantities of flagged pixels that are filtered through the aforementioned steps will be essentially unchanged when varying the threshold $\pm 10\%$. The uncertainties of footpoint regions should depend on the initial boundaries of dimmings. As mentioned in the Section 2.2, we analyze all EUV channels and the corresponding HMI data to acquire the boundaries. Unfortunately, it is very complicated to estimate the errors in these steps.

B. CALCULATING ELECTRIC CURRENT AND ASSOCIATED UNCERTAINTIES

Previous studies (e.g. Liu et al. 2017; Avallone & Sun 2020) neglected the pixels with $|B| < 200$ G when calculating the vertical electric currents from the HMI data to avoid regions with low signal-to-noise ratios. In this study, we have done a series of calculations to check how noise-like regions affect the estimation of electric current. Table 5 shows four results for electric current calculations. The original value of I_z calculated by integrating all pixels in the footpoint regions is shown in the first column (labeled as (1) in the Table 5). The second (2) and third (3) terms are two values of I_z calculated by only considering the pixels with $|B| > 100$ G or $|B| > 200$ G respectively. The time-averaged value of I_z is shown in the last column (labeled as (4) in the Table 5). The results show that removing the weak-field pixels from calculations will reduce the value of I_z . For many events, if we neglect the pixels with $|B| < 200$ G, the I_z^{DC} will decrease by 2 to 4 times when comparing with the original value. The R_z calculated from these different values of I_z is listed in the last group of Table 5. Removing weak-field pixels from calculations will increase the value of R_z . We find that the time-averaged value of I_z is similar to the value of I_z calculated by removing pixels with $|B| < 100$ G, 0.5 to 1 times of the original value. But the time-averaged value of R_z can better help us to distinct two MFR populations, with

or without net current. We finally decide to take the time-averaging value of I_z as our estimations in this study.

Here we also compare three different methods of estimating uncertainties of electric currents. 1) we follow the principle of the error propagation:

$$\sqrt{\delta_{B_x(i,j+2)}^2 + \delta_{B_x(i,j+1)}^2 + \delta_{B_x(i,j-1)}^2 + \delta_{B_x(i,j-2)}^2 + \delta_{B_y(i+2,j)}^2 + \delta_{B_y(i+1,j)}^2 + \delta_{B_y(i-1,j)}^2 + \delta_{B_y(i-2,j)}^2}$$

to attain the δ_{j_z} based on uncertainties from HMI data ($\delta_{B_x}, \delta_{B_y}$). 2) we tried a Monte Carlo simulation to calculate δ_{j_z} by randomly varying transverse field within uncertainties from HMI data. The simulation is conducted with 10^5 iterations. Then the standard deviation of the Gaussian distribution of j_z at each pixel is taken as δ_{j_z} . 3) the standard derivation of the variation of j_z during two hours prior to flare is taken as δ_{j_z} . Table 6 shows three different errors for I_z^{net} , I_z^{DC} and I_z^{RC} . The errors calculated by the propagation equations are always larger than the another two methods. The smallest errors are always from the Monte Carlo simulation. There are no huge difference for three methods. As explained in the Section 2.3.2, the time-averaged value of j_z is selected to calculate electric current. It is suitable to take the standard derivation of j_z during two hours as the errors here.

Table 6. Errors for direct currents inside the 28 MFRs

No.	Date		$\delta_{I_{z,net}}$ (10^{11} A)			$\delta_{I_{z,DC}}$ (10^{11} A)			$\delta_{I_{z,RC}}$ (10^{11} A)		
			EP	MCS	SD	EP	MCS	SD	EP	MCS	SD
1	20100807	<i>FP+</i>	1.88	0.72	1.31	1.40	0.61	0.64	1.27	0.37	0.65
		<i>FP-</i>	1.66	0.64	1.15	1.04	0.63	0.54	1.04	0.47	0.50
2	20110307	<i>FP+</i>	1.85	0.82	1.31	1.23	0.69	0.65	1.34	0.45	0.64
		<i>FP-</i>	1.96	0.78	1.29	1.46	0.63	0.62	1.44	0.47	0.60
3	20110621	<i>FP+</i>	3.16	1.48	1.82	3.77	1.06	1.26	3.73	1.03	1.24
		<i>FP-</i>	3.10	1.29	1.68	3.66	0.93	1.07	3.61	0.90	1.06
4	20110802	<i>FP+</i>	1.66	0.73	0.91	1.09	0.66	0.36	0.99	0.32	0.27
		<i>FP-</i>	1.86	0.62	1.16	1.41	0.59	0.64	1.30	0.18	0.50
5	20110930	<i>FP+</i>	2.33	1.09	1.49	2.11	1.00	0.91	1.98	0.52	0.78
		<i>FP-</i>	2.61	0.62	1.06	2.57	0.58	0.42	2.02	0.18	0.21
6	20120309	<i>FP+</i>	2.64	1.02	1.48	2.72	0.85	0.82	2.63	0.57	0.80
		<i>FP-</i>	2.72	1.14	1.45	2.89	0.83	0.87	2.70	0.77	0.79
7	20120310	<i>FP+</i>	2.50	1.30	1.61	2.36	0.81	0.97	2.32	1.02	0.91
		<i>FP-</i>	2.61	1.24	1.46	2.54	0.87	0.82	2.61	0.87	0.78
8	20120614	<i>FP+</i>	1.90	0.51	0.87	1.37	0.47	0.28	0.78	0.20	0.15
		<i>FP-</i>	2.06	1.33	1.32	1.72	1.16	0.70	1.49	0.64	0.61
9	20120712	<i>FP+</i>	2.81	1.73	1.87	2.97	1.02	1.34	3.23	1.40	1.32
		<i>FP-</i>	2.91	1.68	1.84	3.15	1.00	1.26	2.90	1.36	1.28
10	20130206	<i>FP+</i>	2.35	1.01	1.41	2.11	0.62	0.73	2.06	0.80	0.76
		<i>FP-</i>	2.17	0.99	1.42	1.81	0.81	0.78	1.77	0.56	0.76
11	20130411	<i>FP+</i>	2.98	1.60	1.80	3.40	1.33	1.23	3.32	0.88	1.21
		<i>FP-</i>	1.55	0.53	0.93	0.91	0.36	0.32	0.82	0.59	0.36
12	20130517	<i>FP+</i>	1.72	0.64	1.09	1.13	0.52	0.45	1.12	0.36	0.45
		<i>FP-</i>	2.70	1.33	1.78	2.79	0.62	1.19	2.70	1.17	1.19
13	20130812	<i>FP+</i>	1.23	0.43	0.79	0.60	0.35	0.24	0.57	0.25	0.23
		<i>FP-</i>	1.18	0.40	0.86	0.54	0.30	0.32	0.50	0.26	0.24
14	20130817	<i>FP+</i>	1.45	0.47	0.93	0.80	0.32	0.30	0.74	0.34	0.33
		<i>FP-</i>	2.07	0.75	1.19	1.59	0.47	0.54	1.63	0.59	0.53
15	20130830	<i>FP+</i>	3.05	1.16	1.61	3.55	0.62	0.99	4.55	0.98	0.96
		<i>FP-</i>	3.48	1.92	2.08	4.57	1.67	1.64	3.44	0.95	1.64
16	20131013	<i>FP+</i>	1.79	0.62	1.14	1.21	0.43	0.49	1.10	0.44	0.47
		<i>FP-</i>	1.87	1.07	1.23	1.39	0.88	0.63	1.25	0.60	0.51
17	20140131	<i>FP+</i>	2.10	0.95	1.44	1.68	0.77	0.80	1.63	0.55	0.76
		<i>FP-</i>	2.09	0.87	1.39	1.64	0.55	0.73	1.59	0.68	0.70
18	20140320	<i>FP+</i>	2.03	0.75	1.27	1.55	0.48	0.60	1.54	0.58	0.61
		<i>FP-</i>	1.41	0.55	0.93	0.77	0.43	0.35	0.73	0.34	0.31
19	20140730	<i>FP+</i>	1.10	0.50	1.18	2.00	1.00	0.56	1.10	0.50	0.50
		<i>FP-</i>	1.40	0.40	1.31	1.20	0.40	0.65	1.30	0.30	0.70
20	20140801	<i>FP+</i>	2.06	0.93	1.30	1.60	0.58	0.46	1.56	0.73	0.67
		<i>FP-</i>	1.84	0.61	1.13	1.25	0.39	0.50	1.29	0.48	0.63
21	20140825	<i>FP+</i>	1.62	0.77	1.04	1.02	0.67	0.45	0.95	0.37	0.37
		<i>FP-</i>	1.25	0.57	0.82	0.59	0.47	0.26	0.45	0.32	0.26
22	20140825	<i>FP+</i>	1.70	0.79	1.19	1.09	0.58	0.55	1.08	0.40	0.52
		<i>FP-</i>	1.20	0.50	0.84	0.54	0.36	0.27	0.56	0.34	0.28
23	20140908	<i>FP+</i>	2.17	0.82	1.01	5.47	0.70	0.44	1.78	0.40	0.38
		<i>FP-</i>	2.57	1.39	1.69	2.53	0.94	1.13	2.47	1.02	1.02
24	20140910	<i>FP+</i>	1.85	0.89	1.23	1.37	0.65	0.50	1.29	0.61	0.57
		<i>FP-</i>	2.85	1.28	1.55	3.15	0.95	0.95	2.99	0.87	0.87
25	20140921	<i>FP+</i>	1.72	0.65	1.19	1.10	0.46	0.55	1.12	0.45	0.52
		<i>FP-</i>	1.35	0.38	0.89	0.69	0.26	0.30	0.69	0.27	0.29
26	20141220	<i>FP+</i>	2.22	1.80	1.55	1.86	0.80	0.90	4.23	0.80	0.86
		<i>FP-</i>	2.38	0.70	1.42	2.15	1.50	0.77	2.10	1.20	0.76
27	20150622	<i>FP+</i>	1.77	0.81	1.04	1.22	0.69	0.46	1.11	0.43	0.35
		<i>FP-</i>	3.10	1.44	1.69	3.34	1.08	1.02	3.61	0.96	1.08
28	20151104	<i>FP+</i>	2.52	0.50	1.33	2.30	0.80	0.67	2.49	0.50	0.66
		<i>FP-</i>	2.53	1.00	1.88	2.41	0.70	1.33	2.36	0.50	1.36